

# Reconstruction of Gamma Ray Burst Lightcurves: A Machine/Deep Learning Approach

A. Manchanda<sup>a,\*</sup>, M. G. Dainotti<sup>b,c,d,e,\*\*</sup>, A. Deepu<sup>1</sup>, A. Kaushal<sup>1</sup>, H. Gupta<sup>1</sup>, A. Pollo<sup>ij</sup>, N. Fraija<sup>1</sup>

<sup>a</sup>Department of Physics, Indian Institute of Technology, IITH Road, Near NH-65, Sangareddy, Kandi, Hyderabad, 502284, India

<sup>b</sup>Division of Science, National Astronomical Observatory of Japan, 2-21-1 Osawa, Mitaka, Tokyo, 181-8588, Japan

<sup>c</sup>The Graduate University for Advanced Studies (SOKENDAI), Shonankokusaimura, Hayama, Miura District, Kanagawa, 240-0115, Japan

<sup>d</sup>Space Science Institute, 4765 Walnut St Ste B, Boulder, 80301, CO, USA

<sup>e</sup>Nevada Center for Astrophysics, University of Nevada, 4505 Maryland Parkway, Las Vegas, 89154, NV, USA

<sup>f</sup>Department of Ocean Engineering and Naval Architecture, Indian Institute of Technology, Kharagpur, Paschim Medinipur, Kharagpur, 721302, India

<sup>g</sup>Department of Computer Science and Engineering, UIET-H, Panjab University, Sector 14, Chandigarh, 160014, India

<sup>h</sup>MIT WPU School of Computer Science & Engineering, Survey No, 124, Paud Rd, Kothrud, Pune, 411038, India

<sup>i</sup>Astronomical Observatory of Jagiellonian University in Kraków, Orla 171, Krakow, 30-244, Poland

<sup>j</sup>National Centre for Nuclear Research, Warsaw, 02-093, Poland

<sup>k</sup>National Autonomo University of Mexico, Circuito Interior, Mexico City, 04510,

## Abstract

Gamma-ray bursts (GRBs), which are highly energetic bursts, have been detected at high redshifts ( $z = 9.4$ ) and are pivotal for cosmological research and the study of Population III stars. To address these studies, it is important to identify correlations between the key GRB variables while minimizing uncertainties. This requires comprehensive coverage of GRB Light curves (LCs), which, however, are challenging to obtain given the observational gaps and noise. Those issues often prevent us from precise parameter estimation. In this study, we explore the reconstruction of GRB LCs using three machine learning models: Bidirectional Long Short-Term Memory (Bi-LSTM), Conditional Generative Adversarial Networks (CGAN), and a Sarimax-based Kalman filter. To evaluate these approaches, we also include well-established functional form parametric methods such as the Willingale model (W07) and the non-parametric Gaussian Processes (GPs), expanding upon Dainotti et al. 2023b by applying our techniques to a larger sample of 545 GRBs, covering four different GRB classifications. Our findings reveal that the LSTM model achieves the highest reductions in the uncertainties of the plateau parameters, with decreases of 29% in  $\log T_a$ , 31% in  $\log F_a$  and 40% in  $\alpha$ . In comparison, GPs show a slightly smaller reduction of 22% in both  $\log T_a$  and  $\log F_a$ , and 32% in  $\alpha$  while CGANs exhibit a decrease of 23% in  $\log T_a$ , 24% in  $\log F_a$ , and 31% in  $\alpha$ . The Sarimax-based Kalman filter performs well for well-sampled and flare-free GRBs, but it has problems with reconstruction in more complex cases. It shows a decrease of 14% in  $\log T_a$ , 5% in  $\log F_a$  and 6% in  $\alpha$ . When comparing the relative reductions, the LSTM model consistently shows the largest improvements across all parameters, while the GP and CGAN models achieve reductions that are approximately 10% smaller. The Sarimax-based Kalman filter shows the least improvement, with reductions approximately 15% lower than LSTM. For the subset of 299 Good GRBs, namely with well-defined plateau emission with no flares and bumps, the LSTM model achieved a reduction of approximately 40%, with a percentage increase of 8% compared to the results observed in Dainotti et al. 2023b, which showed the uncertainty reduction of 37% for the W07 model at the 10% noise level. These advancements are essential for using GRBs as standard candles in cosmology, investigating theoretical models, and predicting GRB redshifts through recent cutting-edge machine-learning analysis.

**Keywords:**  $\gamma$ -ray bursts— statistical methods— relativistic processes—cosmology: cosmological parameters— light curve reconstruction

## 1. Introduction

GRBs are brief and highly luminous astrophysical phenomena detectable at remarkable distances (for review, see Kumar and Zhang, 2015), with observations extending up to redshift  $z = 9.4$  (Cucchiara et al., 2011). This property makes GRBs exceptional cosmological tools for probing the early evolution of the universe. A thorough analysis of GRBs also yields essential information about Population III stars, the first generation formed during the epoch of re-ionization. GRB emission

is usually observed in two episodes: the prompt and the afterglow. The prompt phase is interpreted by internal shell collisions or magnetic reconnection and is characterized by having a short duration and high energy. Hence this is detected predominantly in  $\gamma$  rays and X-rays and occasionally in optical wavelengths (Vestrand et al., 2005; Blake et al., 2005; Beskin et al., 2010; Gorbovskoy et al., 2012; Vestrand et al., 2014). During the afterglow phase, which follows the primary episode, the relativistic jet contacts the circumstellar environment, transferring part of its energy. The afterglow is characterized by having a long duration and energies that span a broad spectrum, including X-ray, optical, and sometimes radio bands (Costa et al., 1997; van Paradijs et al., 1997; Piro et al., 1998;

\*Corresponding author, aditii18m@gmail.com

\*\*Corresponding author, maria.dainotti@nao.ac.jp

Gehrels et al., 2009). GRBs have conventionally been categorized into two groups according to the duration of their gamma-ray prompt episode, quantified by  $T_{90}$ . This metric reflects the duration during which 90% of the total background-deducted counts that had been recorded, beginning after the first 5% of counts have been detected (Mazets et al., 1981; Kouveliotou et al., 1993). Short GRBs (SGRBs), defined by  $T_{90} \leq 2s$ , are typically associated with the mergers of compact objects (Duncan and Thompson, 1992; Narayan et al., 1992; Usov, 1992; Thompson, 1994; Levan et al., 2008; Metzger et al., 2011; Bucciantini et al., 2012; Perna et al., 2016). In contrast, long GRBs (LGRBs), with  $T_{90} \geq 2s$ , are linked to the collapse of massive stars (Woosley, 1993; Paczyński, 1998; MacFadyen and Woosley, 1999; Bloom et al., 2002; Hjorth et al., 2003; Woosley and Bloom, 2006; Woosley and Heger, 2006; Kumar et al., 2008; Hjorth and Bloom, 2012; Bucciantini et al., 2008; Cano et al., 2017; Lyman et al., 2017; Perna et al., 2018; Aloy and Obergaulinger, 2021; Ahumada et al., 2021).

The Neil Gehrels Swift Observatory (Swift, Gehrels et al. 2004) is vital for detecting the temporal properties of GRBs. The Swift Burst Alert Telescope (BAT), operating in the 15-150 keV range (Barthelmy et al., 2005), plays a crucial role in quickly detecting prompt emission. It enables a rapid follow-up of the afterglow through the X-ray Telescope (XRT) instrument, which covers the 0.3-10 keV range (Burrows et al., 2005), and the Ultra-Violet Optical Telescope (UVOT 170 - 600 nm, (Roming et al., 2005)). Moreover, Swift's rapid multi-wavelength afterglow follow-up has revealed new characteristics in GRB LCs (Tagliaferri et al., 2005; Nousek et al., 2006; Troja et al., 2007).

Most X-ray LCs have a steep flux decay following the end of the prompt episode, sometimes followed by flares and/or a plateau (Zhang et al., 2006; O'Brien et al., 2006; Nousek et al., 2006; Sakamoto et al., 2007; Liang et al., 2007; Willingale et al., 2007; Dainotti et al., 2008, 2010, 2016, 2017). (Vestrand et al., 2005; Kann et al., 2006; Zeh et al., 2006; Panaitescu and Vestrand, 2008; Kann et al., 2010; Panaitescu and Vestrand, 2011; Kann et al., 2011; Li et al., 2012; Oates et al., 2012; Zaninoni et al., 2013; Margutti et al., 2013; Melandri et al., 2014; Li et al., 2015, 2018a; Si et al., 2018; Dainotti et al., 2020b). The plateau observed in GRB LCs can be modeled using a broken power-law (BPL) (Zhang et al., 2006, 2007; Racusin et al., 2009), a smoothly broken power-law, or the phenomenological model proposed by (W07, Willingale et al. 2007). The W07 model determines critical parameters such as the time at the end of the plateau,  $T_a$ , the corresponding flux,  $F_a$ , and the temporal index after the plateau,  $\alpha_a$ . On the other hand, the BPL model provides  $T_a$ ,  $F_a$ , and the slope of the LC during the plateau,  $\alpha_1$  and after the plateau,  $\alpha_2$ . Section 2.1 details the W07 and the parameters.

The plateau phase is frequently interpreted using the magnetar model (Zhang and Mészáros, 2001), which attributes the emission to dipole radiation generated by the rotational energy of a newly formed neutron star (NS). According to this model, the plateau ends when the NS reaches its critical spin-down timescale. Uncertainties in determining  $T_a$  are often linked to the magnetar spin period and magnetic field uncertainties.

Therefore, precise measurements of  $T_a$  are essential to verify the validity of this model. The plateau phase exhibiting more consistent features across various GRBs, such as length and flatness, have attracted attention due to their potential to establish relevant correlations with the plateau parameters and their application as cosmological tools. (Dainotti et al., 2008, 2010, 2011; Dainotti et al., 2013; Dainotti et al., 2015, 2017; Tang et al., 2019; Wang et al., 2022; Zhao et al., 2019; Liang et al., 2007) and Li et al. 2018b have explored the luminosity at the end of the plateau,  $L_{X,a}$  vs its rest-frame time  $T_{X,a}^*$  (known as the Dainotti relation or 2D L-T relation)<sup>1</sup>. The 2D relation has also been identified in the optical plateau emissions (Dainotti et al., 2020b, 2022b). Within the theoretical magnetar framework, Rowlinson et al. 2014 showed that the X-ray Dainotti relation is reproduced with a slope for  $L_{a,X}-T_{a,X}^*$  of  $-1$ . This correlation has been applied in cosmological research, such as the development of the GRB Hubble diagram, which extends to redshifts greater than  $z > 8$  (Cardone et al., 2009, 2010; Postnikov et al., 2014; Dainotti et al., 2013).

The 2D L-T relation has been further expanded by incorporating the peak prompt luminosity,  $L_{X,peak}$ , resulting in the Dainotti 3D relation (Dainotti et al., 2016, 2017, 2020a, 2022b). This 3D relation has also been successfully applied to constrain cosmological parameters (Dainotti et al., 2023a; Dainotti et al., 2022g; Dainotti et al., 2022b; Cao et al., 2022a,b). Importantly, Dainotti et al. 2022g demonstrated that reducing the uncertainties associated with the plateau emission parameters by 47.5% could achieve the same precision for the cosmological value of  $\Omega_M$  quoted in Betoule et al. 2014 in just 8 years as we have calculated in (Dainotti et al., 2022c; Narendra et al., 2024), if we consider the optical sample and the addition of GRBs for which the redshift has been inferred (Dainotti et al., 2024c,b). This improvement could be realized immediately, compared to the precision that would otherwise require 22 more years of observations under current rates and parameter uncertainties Dainotti et al. 2022g. This highlights the significant potential of a more reliable LCR approach, as it could substantially accelerate progress to reach the same precision achieved by SNe Ia (for details see Dainotti et al., 2020b).

Despite these advancements, GRB LCs with temporal gaps present significant challenges in testing theoretical models, such as the standard fireball model (Panaitescu and Kumar, 2000; Piran, 1999). This model is typically evaluated using closure relations (Willingale et al., 2007; Evans et al., 2009; Racusin et al., 2009; Kumar and Duran, 2010; Srinivasaragavan et al., 2020; Dainotti et al., 2021; Ryan et al., 2020; Tak et al., 2019), which involve the temporal ( $\alpha$ ) and spectral ( $\beta$ ) index of the afterglow. The value of  $\alpha$  may correspond to either  $\alpha_1$  or  $\alpha_2$ , depending on the segment of the analyzed LC, while  $\beta$  must be measured for the same time window as  $\alpha$ . An accurate assessment of these factors is essential for evaluating the fireball model and categorizing GRBs according to their morphology.

However, gaps occurring due to satellite orbital periods, lack of fast follow-up studies, meteorological turbulence, and instrumental errors, complicate these measurements. To address

<sup>1</sup>the rest-frame time is denoted with an asterisk

these challenges, further improvement in the understanding of GRBs requires extensive data coverage and the development of a reliable taxonomy of GRB classes. Such efforts could considerably improve studies on GRB populations, their cosmological evolution, emission mechanisms, and/or progenitors.

Thus, here we tackle the Light Curve Reconstruction (LCR), which provides a novel approach to address the challenge of temporal gaps in LCs. Various approaches have been developed to address gaps in observational data. Dainotti et al. 2023b introduced a stochastic reconstruction technique using existing models and GPs, reducing uncertainties for key GRB parameters. Sourav et al. 2023 proposed using BiLSTM for LCR. Both methods demonstrated improved performance over traditional methods. However, deviations are observed towards the end of the GRB LC in the reconstructions generated by the aforementioned BiLSTM model. In contrast, our proposed LSTM model demonstrates the ability to reconstruct even the terminal segments accurately, ensuring greater consistency with the original LC.

Recent advances in machine learning have further pushed the boundaries of LCR. For example, Demianenko et al. 2023 examined the application of neural network-based methods, including Bayesian neural networks, multilayer perceptrons, and normalizing flows, to obtain approximate findings of a single LC. These methods were tested on the light curves of Supernovae type 1a taken from Zwicky Transient Facility Bright Transient Survey and simulated PLAsTiCC. These methods demonstrated that even with limited observations, neural networks could significantly enhance the quality of the reconstruction in comparison to state-of-the-art models. Moreover, they are computationally efficient, outperforming GPs considering the speed, and were found to be effective for subsequent tasks like peak identification and transient classification.

Building on these advancements, this work focuses on furthering the utilization of deep learning techniques in studying and researching GRB LCR. Specifically, we explore the potential of LSTMs, CGAN, and the Kalman Sarimax models. This paper, highlights their strengths and limitations and performs a comparative analysis to assess their performance. This paper is divided into the following sections: sec. §2 provides a comprehensive detailing of the dataset utilized and the various models employed for the reconstruction of GRB LCs, including the W07 model, GP, LSTM, CGAN, and the Sarimax-based Kalman method. Sec. §3 presents the reconstruction results and highlights the percentage decrease in uncertainty of the plateau parameters achieved through each model. Sec. §4 summarizes the findings and provides concluding remarks on the effectiveness of the models. An appendix is included at the end, describing another three models: decision trees, random forests, and a hybrid model that combines random forests as a base with GP trained over it. These models are discussed to illustrate their limitations, as they did not yield satisfactory reconstruction results at the present stage.

## 2. Methodology

To account for the missing data points in the LC, we adopt five approaches detailed below.

### 2.1. Dataset and the Willingale model

In this study, we used a data sample of 545 GRBs (refer to Table 1 from Srinivasaragavan et al. 2020; Dainotti et al. 2020a characterized by X-ray plateaus, including 230 from known redshift and 315 without known redshift taken from (Dainotti et al., 2024c,b; Narendra et al., 2024). The data was originally sourced from the Swift BAT-XRT repository (Evans et al., 2009, 2007).

The LC of the GRBs are modeled using the W07 function, defined in Eq. 1 from Willingale et al. 2007:

$$f(t) = \begin{cases} F_i \exp\left(\alpha_i \left(1 - \frac{t}{T_i}\right)\right) \exp\left(-\frac{t_i}{t}\right) & \text{for } t < T_i, \\ F_i \left(\frac{t}{T_i}\right)^{-\alpha_i} \exp\left(-\frac{t_i}{t}\right) & \text{for } t \geq T_i. \end{cases} \quad (1)$$

In this function,  $T_i$  and  $F_i$  represent the time and the flux, respectively, either at the end of the prompt emission ( $p$ ) or at the end of the plateau phase ( $a$ ). The temporal index parameter after  $T_i$  is defined as  $\alpha_i$ . The time  $t_i$  marks the initial rise phase, while  $t_a$  is denoted for the afterglow emission.

The LCs in our sample have been preprocessed to exclude the prompt emission phase, as it is highly variable and complex to model accurately. As a result, the dataset focuses on the plateau and afterglow phases. The GRBs were then classified based on their afterglow features.

The classification schemes divided the GRBs into four categories:

- **Good GRBs:** GRBs with a good approximation to the W07 model, constituting 55.3% of the sample.
- **Flares/Bumps:** GRBs exhibiting flares and bumps throughout the afterglow region, reaching to 24.06%.
- **Break:** GRBs with a single break at the end of the LC constitute 13.14% of the sample.
- **Flares/Bumps + Double Break:** GRBs exhibiting both flares/bumps and double break comprise 7.5% of the entire sample.

This classification was adapted from a similar methodology presented by (Dainotti et al., 2023b).

These classifications were made based on the GRB afterglow LCs, with each LC being compared to the W07 function model. The parameter values for each GRB LC were obtained from Srinivasaragavan et al. 2020. Fig. 1 displays the LCs for all classes, modeled with W07 model.

GRB NAME	$z$	$T_{90}$	$\frac{T_{90}}{(1+z)}$	LONG/SHORT	Type	Reference
GRB060510B	4.90	262.95	44.57	L	XRR	[1]
GRB060526	3.22	275.20	65.21	L	XRR	[2]
GRB060604	2.14	96.00	30.62	L	XRR	[1]
GRB060605	3.73	539.12	113.91	L	XRR	[2]
GRB060607A	3.07	102.20	25.11	SEE	SEE	[1]
GRB060614	0.13	109.104	96.95	SEE	SEE/XRR	[1], [3]
GRB060707	3.14	66.65	15.08	L	XRR	[2]
GRB060708	1.92	9.96	3.41	L	XRR	[1]
GRB060714	2.71	116.06	31.28	L	XRR	[2]

Table 1: Sample of all 545 GRBs, including redshift  $z$ , observer-frame burst duration  $T_{90}$  and rest-frame duration  $\frac{T_{90}}{(1+z)}$ , long vs. short classification, GRB type, and reference. Full table is uploaded online. References: [1] Sakamoto et al. 2008; [2] Bi et al. 2018; [3] Dainotti et al. 2022a.

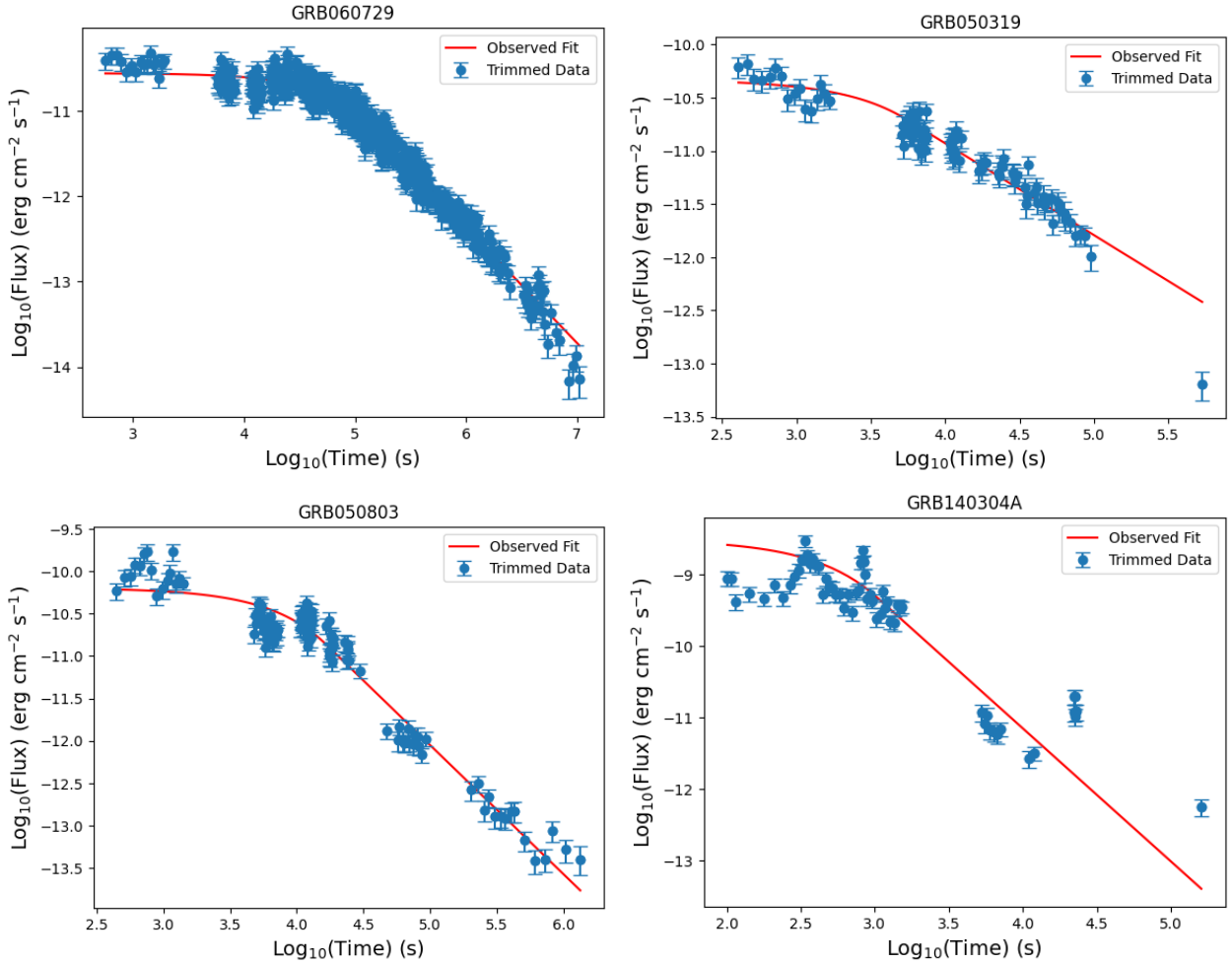


Figure 1: The GRB LCs are divided into 4 classes depending on the afterglow feature: i) Good GRBs (upper left); ii) GRB LCs with a break towards the end (upper right); iii) Flares or Bumps in the afterglow (bottom left); iv) Flares or Bumps with a Double Break towards the end of the LC (bottom right).

## 2.2. Reconstruction with the Willingale model

In this section, we adhere to the methodology outlined in (Dainotti et al., 2023b) to reconstruct the LCs using the W07 model. However, our approach further extends the analysis by including all classes of the GRBs, allowing for a more extensive analysis of the model across different GRB categories.

The flux residual for each LC is calculated as the difference between the logarithm flux of the original LC and the logarithmic flux value predicted by the W07 fit at a given time  $t$  (in  $\log_{10}$  scale).

$$\log_{10} F_{\text{res}} = \log_{10} F_{\text{obs}}(t) - \log_{10} f(t). \quad (2)$$

where  $\log_{10} F_{\text{res}}$  is the flux computed as the residual, while  $F_{\text{obs}}$  is the observed flux and  $f(t)$  is the W07 functional form at the given time  $t$ .

We then perform the same steps as described, generating histograms of the residuals for each GRB and fitting a Gaussian distribution, as a first approximation, to those residuals as presented in Fig. 2. The reconstructed flux at each time point is calculated by adding noise, sampled from the residual distribution, to the flux predicted by the W07 model:

$$\log_{10} F_{\text{recon}}(t) = \log_{10} f(t) + (1 + n) \times \text{RVN}. \quad (3)$$

where  $\log_{10} F_{\text{recon}}(t)$  represents the reconstructed flux at time  $t$ ,  $f(t)$  denotes the W07 flux at time  $t$ ,  $n$  is the noise level and RVN refers to the random variate sampled from the Normal (Gaussian) distribution.

We evaluate the reconstruction at 10% and 20% noise levels. This method ensures the reconstructed data points are statistically consistent with the best-fit W07 model as the initially observed points. We reconstruct time series using a logarithmic distribution via the *geomspace* function and perform 100 times MCMC calculations for each GRB to guarantee stability of the model. The combined data (original and reconstructed points) is then refitted using a least-squares regression with the *minimize()* function from the *lmfit* library, providing the new fitting parameters and uncertainties of the reconstructed LCs.

## 2.3. GP with hyperparameter tuning

GP regression is a probabilistic, non-parametric approach designed for regression tasks. The probabilistic nature of the GP model allows for the likelihood of the prediction instead of producing a singular prediction. The method relies on Bayesian inference, where the prior—based on trends in the observed data—is updated to compute a posterior that aligns with the data. The model prediction is bounded by the confidence interval, which defines the region of likelihood of the prediction.

A key component of GP is the kernel, or covariance function, which measures the similarity between data points. For our analysis, we utilize a Radial Basis Function kernel combined with a White Noise kernel because we assume that the flux noises are independent and identically normally distributed.

To implement GPs, we utilized the *GaussianProcessRegressor* from *scikit-learn*, enabling prediction with prior knowledge of the GP without its' prior fitting. The standardized prior indicates that the mean is centered at zero. The GP regression

model was fitted with the built-in *fit* function to our data and the reconstruction of data points was done using the in-built *predict* function.

We have selected a 95% confidence interval to reconstruct the LC using GP. Using the form of the function derived by the Gaussian Regressor (built-in function in Python), we avoid the distribution of the data points in the GPs by conducting 100 MCMC simulations of the reconstructed LC for each distinct LC. Next, the value along with its corresponding uncertainty was randomly chosen.

To implement GPs for LCR, we tune two primary hyperparameters: *alpha* and *n\_restarts\_optimizer*.

*alpha* is a value added to the kernel matrix's diagonal during fitting. This fine tune parameter helps avoid potential numerical issues, shown in the left panel of Fig. 3 by ensuring the matrix remains positive and definite. Additionally, *alpha* can be interpreted as the variance of extra Gaussian measurement noise on the training observations. The default value is  $1e-10$ . A larger *alpha* value is frequently required to avoid overfitting in cases where the data is noisy. In other words, to reduce the bumps seen in the left panel of Fig. 3. *n\_restarts\_optimizer* denotes the number of times the optimizer restarts to find the kernel parameters that maximize the log-marginal likelihood. This procedure guarantees a more reliable optimization of the kernel's parameters and aids in avoiding local minima.

In our data, out of the total sample of 545 GRBs, a very small subset containing 9 GRBs with redshifts and 15 GRBs without redshift exhibited significant temporal gaps, defined as time intervals greater than 0.5 (in  $\log_{10}$  scale). As Figure 3a shows, the GP Regressor overfitted these data points, resulting in erratic predictions and excessively wide 95% confidence intervals. This erratic behavior suggested the need for optimal values for *alpha* and *n\_restarts\_optimizer* by employing GridSearchCV for hyperparameter tuning.

GridSearchCV uses 5-fold cross-validation to assess model performance as it iteratively searches through a predefined set of hyperparameters. It exhaustively tests all possible combinations of the specified hyperparameters and selects the combination that results in the best performance according to a chosen metric.

After tuning the hyperparameters with GridSearchCV, we fit the GP Regressor to the data. The optimized model achieved improved reconstruction of the LCs, as shown in Figure 3b.

## 2.4. Long Short Term Memory Neural Network

LSTM (Hochreiter and Schmidhuber, 1997) is a form of Recurrent neural network that performs well in sequence prediction, through its ability to capture long-term dependencies. Unlike traditional neural networks, LSTM incorporates feedback connections, allowing it to process entire data sequences rather than just individual data points. This distinctive architecture equips LSTM with the ability to effectively learn and retain crucial information over time, making it a highly capable deep learning tool well-suited for applications in the fields of speech recognition, language translation, time series forecasting, and more.

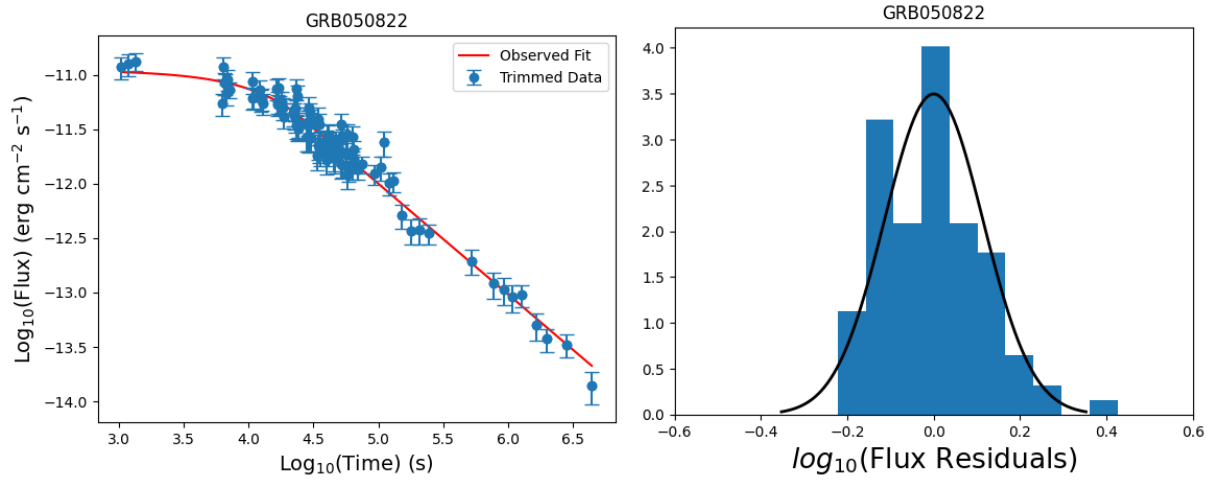


Figure 2: The left image shows the LC of GRB050822 starting from the plateau emission, and the best-fit W07 model is displayed in red. The right plot shows the  $\log(\text{flux})$  residual histogram and the best fit Gaussian distribution is displayed in black.

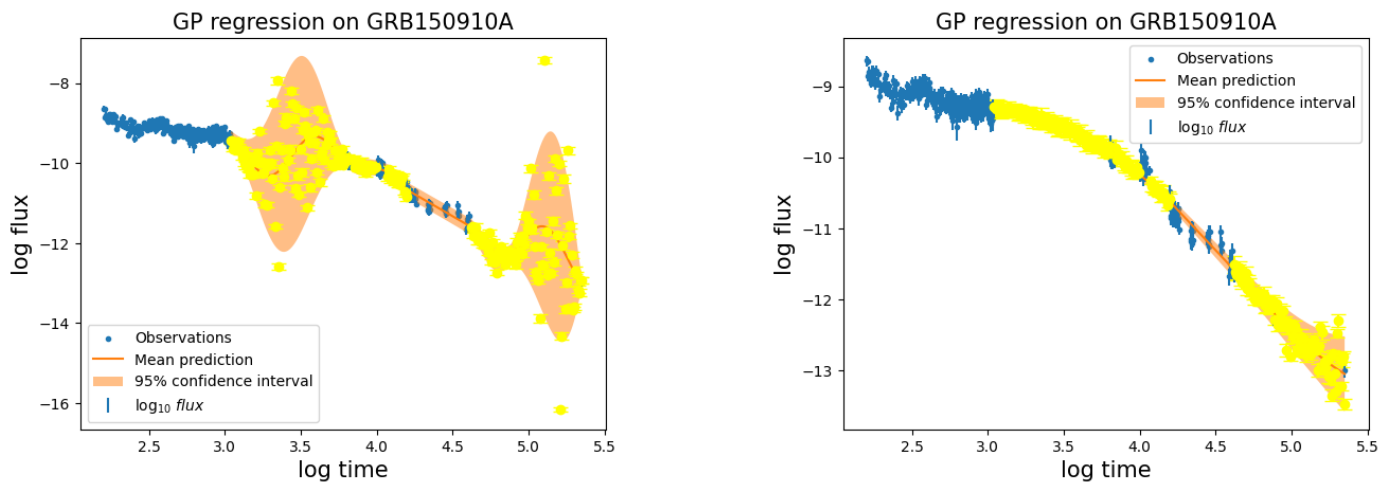


Figure 3: Comparison of LCs before and after hyperparameter tuning.

The main feature of an LSTM is its memory cell, which is managed by three essential gates: the Input gate, the Forget gate, and the Output gate. These gates determine which information is added, removed, and output from the memory cell to effectively learn long-range relationships within the data.

In an LSTM network, a hidden state functions as the short-term memory, capturing information across time steps. This combination allows the LSTM to effectively maintain context and adjust its memory in response to new inputs, facilitating its ability to learn complex patterns across long sequences.

LSTM networks have proven valuable in astrophysics, particularly for time-series data analysis of dynamic celestial phenomena. An example is the LSTM-FCNN model, which combines LSTM and a fully connected neural network to measure time delays in strongly lensed Type Ia supernovae, crucial for measuring the Hubble constant (Huber and Suyu, 2024). Furthermore, LSTMs have been applied for solar flare prediction from active regions (Liu et al., 2019), effectively predicting them using time-series analysis. Both methods demonstrate that LSTMs outperform traditional machine learning models in astrophysical applications.

In our model, we use bidirectional LSTM (BiLSTM) (Graves et al. (2005)) to reconstruct the GRB LCs. The BiLSTM architecture extends the standard LSTM by processing the input data sequence in both forward and reverse directions, allowing it to capture temporal dependencies more effectively. This is particularly useful for GRB LCs, which feature complex temporal patterns such as flares and breaks. BiLSTMs also excel at handling missing data by learning from surrounding observations, enabling accurate imputation. The basic structure of the LSTM is described below and is also shown in Fig. 4 All the variables and symbols are defined in Table 2.

Symbol	Variable
$t$	Time
$x'_t$	Input sequence
$h'_t$	Hidden state
$h'_{t-1}$	Previous hidden state
$C_t$	Cell state
$C'_{t-1}$	Previous cell state
$f'_t$	Forget gate
$i'_t$	Input gate
$o'_t$	Output gate
$W'_f$	Forget gate weights
$W'_i$	Input gate weights
$W'_o$	Output gate weights
$b'_f$	Forget gate bias
$b'_i$	Input gate bias
$b'_o$	Output gate bias

Table 2: List of variables and symbols used in the LSTM model.

- **Input Gate:** It controls the decision of which new information should be incorporated in the cell state. The input is denoted with  $i$ . It computes a gating signal ( $i'_t$ ) using a

sigmoid activation function applied to the weighted combination of current input ( $x'_t$ ) and the previously hidden stage ( $h'_{t-1}$ ), where  $t$  denotes the time, along with a trainable weight ( $W'_i$ ) and bias ( $b'_i$ ):

$$i'_t = \sigma(W'_i \cdot [h'_{t-1}, x'_t] + b'_i). \quad (4)$$

- **Forget Gate:** It determines the amount of the previous memory cell ( $C_{t-1}$ ) should be discarded or retained. The forget gate is denoted with  $f$ . This is also computed using a sigmoid activation function. The gate output is between 0 and 1, where a value close to 0 indicates that the information must be forgotten:

$$f'_t = \sigma(W'_f \cdot [h'_{t-1}, x'_t] + b'_f). \quad (5)$$

- **Cell State Update:** It is responsible for combining the retained information from the previous cell state and the new candidate memory. This update is governed by both the input and forget gates. The forget gate determines how much of the previous memory ( $C'_{(t-1)}$ ) is preserved, while the input gate controls the amount of new information to be added:

$$C'_t = f'_t \cdot C'_{t-1} + i'_t \cdot \tilde{C}'_t. \quad (6)$$

- **Output Gate:** It specifies the portion of the updated cell state to be passed as the hidden state at the current time step. This is also computed using the sigmoid activation function:

$$o'_t = \sigma(W'_o \cdot [h'_{t-1}, x'_t] + b'_o). \quad (7)$$

where  $o'$  denotes the output gate.

Finally, the updated cell state is passed through the hyperbolic tangent function, and the final hidden state is computed as:

$$f'_t = o'_t \cdot \tanh C'_t. \quad (8)$$

In BiLSTM, the input sequence is processed in both forward and reverse directions. The forward LSTM processes the set from the first to the last time step, learning dependencies from the past, while the backward LSTM processes the set from the end, retrieving information from future time steps. Each LSTM layer independently computes the gating signals, hidden and cell states, as described earlier. The outputs from the forward and backward LSTMs are then merged at each time instance to form the final output:

$$h_t^{\text{BiLSTM}} = [h_t^{\text{forward}}, h_t^{\text{backward}}]. \quad (9)$$

In our model, the GRB LCs were preprocessed by converting the flux and time data into a symmetric log scale, improving the model's ability to handle values that span multiple orders of magnitude. The dataset was divided into a 70:30 split for training and validation.

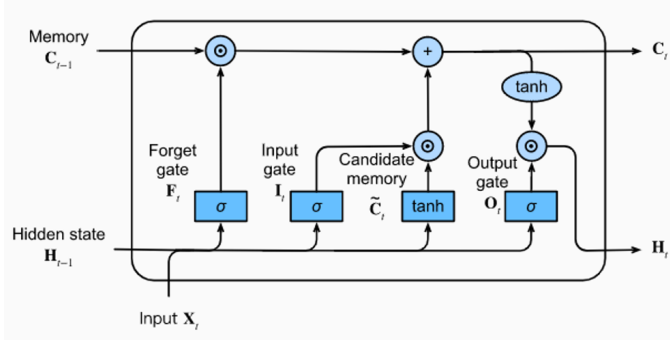


Figure 4: The flow chart of the LSTM Model.

For hyperparameter optimization, *Optuna* (Akiba et al., 2019) was employed to fine-tune important parameters, including the number of BiLSTM layers and the count of hidden units. The architecture consists of BiLSTM layers to capture both forward and backward temporal dependencies, followed by a dense layer with Rectified Linear Unit (ReLU) activation to help the LSTM model learn complex features of flares and breaks in the LC. For GRBs with fewer than 10 data points, linear interpolation was used for upsampling the data, ensuring the model could be trained even on smaller datasets. The model was trained for 100 epochs using the *Adam optimizer*, with performance evaluated using the metric Mean Squared Error. The timestep is taken as 1.

Early stopping criteria was used to prevent overfitting by terminating training when the validation loss fails to improve after a set number of epochs. *ReduceLROnPlateau*, a callback function in Keras is used to reduce the learning rate when the validation loss plateaued, to further optimize the learning process. Validation loss is a measure of how well the model performs on the validation dataset. In this case, the validation loss is calculated using Mean Squared Error (MSE), which represents the average squared difference between the predicted and actual values. The model was developed and trained utilizing the TensorFlow and Keras libraries.

## 2.5. Conditional Generative Adversarial Networks

GANs provide an innovative approach to reconstructing the dataset. These adversarial networks are advantageous over traditional models, bypassing traditional Markov chains during learning (Mirza and Osindero, 2014), only to include it during backpropagation of the gradients. The networks are referred to as generative models and are particularly useful when dealing with complex data distribution, reducing overfitting by incorporating a dual model approach.

These adversarial networks consist of a generator model  $G(z)$  and a discriminator model  $D(x)$  working harmoniously. Both the generator and the discriminator try to improve their results and if the generator constructs more real samples  $x$  from random noise  $z$ , it becomes challenging for the discriminator to distinguish between the real data and the synthetic data. Their adversarial relationship is mathematically described in Eq.10:

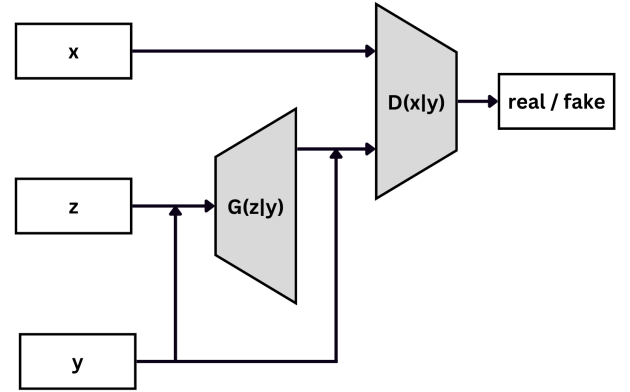


Figure 5: A flow chart showing the CGAN model.

$$\min_G \max_D V(D, G) = \mathbb{E}_{x \sim q(x)} [\log D(x)] + \mathbb{E}_{z \sim r(z)} [\log(1 - D(G(z)))], \quad (10)$$

where the  $\mathbb{E}_{x \sim q(x)} [\log D(x)]$  term denotes the expected value,  $\mathbb{E}$ , of  $\log D(x)$ , where  $x$  is sampled from the observed data distribution  $q(x)$ . Likewise,  $\mathbb{E}_{z \sim r(z)} [\log(1 - D(G(z)))]$  is the expected value of  $\log(1 - D(G(z)))$ , where  $z$  is sampled from the input noise distribution  $r(z)$  of the generator  $G(z)$ .

The CGANs extend this architecture by incorporating a condition set  $y$  into both the generator and discriminator, guiding the data generation process. The architecture of CGAN (as seen in Fig.5) comprises a generator  $G(z|y)$  with two inputs: a condition set  $y$  and a random noise vector  $z$ , and a conditioned discriminator  $D(x|y)$  on  $y$  (Torzadehmahani et al., 2019). The goal of the generator is to create new samples that closely resemble the original samples by using the noise and the condition set as input. After the generation of samples, these, along with the real samples are fed into the discriminator. The objective for the discriminator is to effectively classify between the generated and the real samples, retrospectively training the generator and discriminator in the process. It is mathematically represented in Eq.11:

$$\min_G \max_D V(D, G) = \mathbb{E}_{x \sim q(x)} [\log D(x, y)] + \mathbb{E}_{z \sim r(z)} [\log(1 - D(G(z|y), y))]. \quad (11)$$

In our implementation, the generator begins with a dense layer containing 256 neurons and the *Leaky-ReLU* Linear Unit (*Leaky-ReLU*) activation function (Xu et al., 2015). The *Leaky-ReLU* activation function works by extending the domain values for *ReLU* to incorporate negative values. It includes a positive slope  $m$  and comparatively a small negative slope  $\alpha m$ , preventing the occurrences of dead neurons. In our case,  $\alpha$  is taken to be  $1e - 2$ . Following the dense layer, we utilized two Convolution-1D layers with 64 and 16 filter sizes, respectively.



Paired with *ReLU* activation, these Convolution-1D layers enhance the feature extraction process, ensuring distinct, high-quality features. The preprocessing for flux and time values is by converting them to a symmetric logarithmic scale and further linearly scaling to  $[0, 1]$  scale using *Min-Max Scaler*. The time values act as condition sets for the CGAN, the flux values provide the real data and the noise set contains random uniform noise samples from 0 to 1 covering the whole domain. The discriminator is designed as a generator, ensuring the crucial balance of model complexities and removing the superiority of one model over the other. The generator loss is calculated using the cross-entropy loss between the fake and real data samples, improving the mimicking ability of the generator. This results in reliable data augmentation capabilities for the reconstruction of data.

The proposed method makes use of TensorFlow and Keras libraries for its implementation. The Adam optimizer (Kingma and Ba, 2014) was used to train the model, optimizing the loss function at a learning rate of  $1e - 4$ .

## 2.6. SARIMAX-based Kalman Smoothing Model

We researched the Seasonal Autoregressive Integrated Moving Average with Exogenous Regressors (SARIMAX), Kalman smoothing, and how integrating both models helps in the reconstruction of the GRB LCs. This combination is quite effective since it combines the statistical capability of SARIMAX for time-series modeling with the refinement capabilities of Kalman smoothing, which considers the entire data for the smoothing process.

The time and flux data read from each CSV file is preprocessed by transforming them into the logarithmic domain to stabilize variance and enhance the relationship between time and flux. This ensures computational stability. The lack of data points caused the model to predict GRB fluxes deviating from the true flux values towards the end. This issue was resolved by appending flux values using linear interpolation at flux gaps greater than a certain threshold.

The SARIMAX model is employed to capture the temporal dependencies, trends, and noise in the observed flux data. An ARIMA model of order  $(p,d,q)$  is tuned accordingly to model the LC's temporal dynamics. In our model, we applied Kalman smoothing to refine the SARIMAX output. Kalman smoothing works in such a way that it estimates the system's state using measurements from both past and future time steps. Let  $\mathbf{x}_t$  denote the state vector at time  $t$ , modeled as:

$$\mathbf{x}_t = \mathbf{A}\mathbf{x}_{t-1} + \mathbf{B}\mathbf{u}_t + \mathbf{w}_t, \quad (12)$$

where  $\mathbf{A}$  is the state transition matrix,  $\mathbf{u}_t$  is the control input, and  $\mathbf{w}_t \sim \mathcal{N}(\mathbf{0}, \mathbf{Q})$  represents process noise.

The observation  $\mathbf{y}_t$  is modeled as:

$$\mathbf{y}_t = \mathbf{C}\mathbf{x}_t + \mathbf{v}_t, \quad (13)$$

where  $\mathbf{C}$  is the observation matrix and  $\mathbf{v}_t \sim \mathcal{N}(\mathbf{0}, \mathbf{R})$  represents measurement noise.

The Kalman smoothing algorithm minimizes the mean squared error of state estimates, yielding a refined sequence of

flux values  $\hat{\mathbf{F}}_t$ . After Kalman smoothing, uncertainties were added (as seen in the model flow Fig.6).

The model was implemented using Python libraries such as Statsmodels and Scipy for statistical modeling and Matplotlib for visualization. The SARIMAX fitting is optimized for computational efficiency, and Kalman smoothing is applied using its state-space formulation. The confidence interval bounds were smoothed using a *1D Gaussian filter* to ensure continuity.

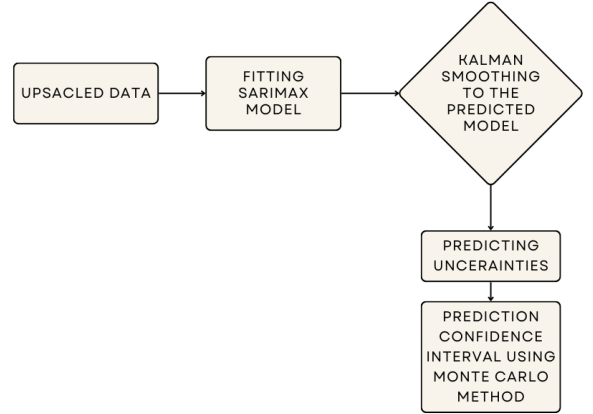


Figure 6: A flow-chart showing the SARIMA+Kalman model.

## 2.7. Uncertainty and Confidence Interval

The uncertainty in the reconstructed flux values was estimated by fitting a Gaussian distribution to the flux residuals, defined as the difference between the original data and the reconstructed data. This Gaussian distribution provides a probabilistic model of the noise. Random noise samples were drawn from this distribution and added to the model's mean prediction to generate realistic flux variations.

To account for variability, we performed Monte Carlo simulations with 1000 iterations. For each iteration, random noise was sampled for each reconstructed data point and added to the corresponding flux value. This process resulted in multiple realizations of the reconstructed LC, capturing the statistical uncertainty of the predictions.

The mean of these realizations was computed to represent the final reconstructed flux. The 95% confidence intervals were determined by calculating the 2.5th and 97.5th percentiles, denoted with  $P$ , of the realizations for each time point, providing a reliable measure of uncertainty for the reconstructed data:

$$CI_{95} = [Percentile_{2.5}, Percentile_{97.5}]. \quad (14)$$

## 3. Results

### 3.1. Results from the Willingale Model

One of the objectives of LCR is to observe a decrease in the uncertainty of the model parameters. To assess this, we com-

GRB ID	$EF_{\log_{10}(T_i)}$	$EF_{\log_{10}(F_i)}$	$EF_{\alpha_i}$	$EF_{\log_{10}(T_i)}$ RC	$EF_{\log_{10}(F_i)}$ RC	$EF_{\alpha_i}$ RC	% $\log_{10}(T_i)$	% $\log_{10}(F_i)$	% $\alpha_i$
				10% noise					
050712	0.018	0.005	0.044	0.014	0.003	0.030	-24.4	-24.3	-30.81
050318	0.010	0.005	0.045	0.007	0.004	0.031	-27.37	-26.84	-30.31
050416A	0.023	0.004	0.017	0.015	0.003	0.011	-33.78	-35.56	-32.83
050607	0.021	0.005	0.044	0.016	0.003	0.026	-22.67	-24.94	-41.21
050713A	0.010	0.002	0.017	0.008	0.002	0.010	-20.17	-17.78	-39.53
050822	0.010	0.003	0.025	0.007	0.002	0.014	-31.94	-35.63	-43.57
050824	0.025	0.005	0.094	0.017	0.003	0.067	-31.71	-30.58	-28.65
050826	0.029	0.018	0.130	0.028	0.019	0.244	-3.2	4.42	87.12
050915B	0.035	0.008	0.115	0.021	0.004	0.064	-39.75	-40.53	-44.02
051016A	0.032	0.005	0.050	0.019	0.003	0.024	-39.15	-30.98	-50.75
051109A	0.011	0.004	0.015	0.005	0.001	0.010	-53.27	-60.46	-34.46
051221A	0.020	0.005	0.050	0.015	0.004	0.032	-22.97	-22.95	-36.31
060105	0.003	0.001	0.007	0.002	0.001	0.003	-16.32	-14	-54.95
060108	0.023	0.006	0.071	0.017	0.004	0.045	-27.66	-32.17	-35.51
060109	0.013	0.005	0.056	0.008	0.002	0.025	-38.75	-43.56	-54.61
060124	0.008	0.004	0.011	0.005	0.002	0.007	-28.24	-30.42	-38.95
060218	0.027	0.013	0.082	0.011	0.004	0.054	-58.97	-69.23	-33.23
060306	0.012	0.003	0.024	0.009	0.002	0.017	-19.57	-27.27	-27.64
060418	0.018	0.005	0.030	0.010	0.003	0.010	-42.33	-31.03	-65.32
060421	0.040	0.010	0.086	0.022	0.006	0.042	-44.67	-36.84	-51.39
				20% noise					
050712	0.018	0.005	0.044	0.015	0.004	0.027	-15.25	-12.92	-37.96
050318	0.010	0.005	0.045	0.008	0.004	0.034	-22.4	-20.98	-24.55
050416A	0.023	0.004	0.017	0.015	0.002	0.011	-34.8	-36.36	-33.54
050607	0.021	0.005	0.044	0.017	0.004	0.029	-17.76	-17.2	-33.21
050713A	0.010	0.002	0.017	0.009	0.002	0.011	-8.35	-5.32	-31.91
050822	0.010	0.003	0.025	0.008	0.002	0.015	-23.64	-28.26	-40.66
050824	0.025	0.005	0.094	0.014	0.003	0.054	-42.35	-38.29	-42.01
050826	0.029	0.018	0.130	0.025	0.017	0.204	-13.66	-9.27	56.65
050915B	0.035	0.008	0.115	0.025	0.005	0.072	-29.85	-33.46	-36.95
051016A	0.032	0.005	0.050	0.022	0.004	0.027	-30.27	-22.06	-46.52
051109A	0.011	0.004	0.015	0.006	0.002	0.011	-47.31	-56.21	-28.49
051221A	0.020	0.005	0.050	0.013	0.003	0.032	-31.7	-31.19	-36.7
060105	0.003	0.001	0.007	0.003	0.001	0.003	-12.17	-10.06	-52.77
060108	0.023	0.006	0.071	0.023	0.005	0.048	-2.09	-17.22	-31.66
060109	0.013	0.005	0.056	0.008	0.002	0.025	-37.64	-43.34	-54.66
060124	0.008	0.004	0.011	0.006	0.003	0.006	-24.41	-25.5	-42.03
060218	0.027	0.013	0.082	0.012	0.004	0.060	-55.85	-65.26	-26.58
060306	0.012	0.003	0.024	0.008	0.002	0.016	-28.44	-30.43	-31.78
060418	0.018	0.005	0.030	0.011	0.003	0.011	-36.28	-23.23	-62.34
060421	0.040	0.010	0.086	0.023	0.006	0.039	-42.01	-37.1	-54.69

Table 3: The W07 error fractions of  $\log_{10}(T_a)$ ,  $\log_{10}(F_a)$  and  $\alpha_a$  before and after reconstruction (with relative percentage decrease in error for all three parameters) at 10% and 20% noise level. Columns first, second and third provide error fraction for original W07 fit, the successive columns fourth, fifth and sixth show the error fraction for the W07 fit after LCs reconstruction. Columns seventh, eighth, ninth show percentage decrease in the error fraction after the reconstruction. The full table will be available online.

pute the error fractions, denoted with  $E$ , for each model parameter in both the original and reconstructed fits. The error fractions for the three Willingale parameters as described in Dainotti et al. 2023b are represented in Equations 15, 16, and 17:

$$EF_{\log_{10}(T_a)} = \left| \frac{\Delta \log_{10}(T_a)}{\log_{10}(T_a)} \right|, \quad (15)$$

$$EF_{\log_{10}(F_a)} = \left| \frac{\Delta \log_{10}(F_a)}{\log_{10}(F_a)} \right|, \quad (16)$$

$$EF_{\alpha_a} = \left| \frac{\Delta \alpha_a}{\alpha_a} \right|. \quad (17)$$

To assess the improvement in the fit after reconstruction, we calculate the percentage reduction in the error fractions:

$$\%_{DEC} = \frac{|EF_X^{\text{after}}| - |EF_X^{\text{before}}|}{|EF_X^{\text{before}}|} \times 100. \quad (18)$$

The reconstruction results for the four classes of GRBs under 10% and 20% noise levels are illustrated in Figs. 7 and 8. For each GRB type, the reconstructed LCs demonstrate how increasing noise levels affect the spread of data points around the W07 fit. As shown in Fig. 7, at 10% noise, the reconstructed points cluster closer to the W07 fit, while at 20% noise, as shown in 8, the points exhibit a greater dispersion, reflecting the higher uncertainty.

Table 3 presents the calculated error fractions before and after reconstruction for the W07 model, applied to the entire set of 545 Good GRBs at 10% and 20% noise levels. The initial three columns display the error fractions for each W07 parameter from the original fit, while the subsequent three columns show the error fractions for the parameters after reconstruction using the new fit. These values are computed as averages from the 100 iterations, as previously stated.

The last three columns of Table 3 show the percentage change in the error fraction after reconstruction for the two noise levels. Our analysis reveals that the error fraction for the reconstructed parameters is smaller than that of the original parameters. For the 10% noise level, the error fraction decreases by 25% for the  $\log(T_a)$  parameter, a 26% decrease for the  $\log(F_a)$  parameter, and a 36% decrease for the  $\alpha$  parameter. For the 20% noise level, we obtain a 21% decrease in error fraction on the  $\log(T_a)$  parameter, a 23% decrease for the  $\log(F_a)$  parameter, and a 35% decrease for the  $\alpha$  parameter.

As anticipated, increasing the noise level generally leads to higher uncertainty as a result of the wider uncertainty around the best-fit line. However, in our case, the decrease in uncertainty does not follow this pattern with increasing noise level. This is because we are considering the entire sample. The data points deviate significantly from the model function, for GRBs exhibiting flares and breaks. As a result, with larger noise levels, the decrease in uncertainty is less pronounced.

The histograms of Fig. 9 show the distribution of percentage decrease (the top panel represents the 10% noise level, while the lower panel displays the 20% noise level) for the three W07 parameters. As shown, the reconstruction results in reduced errors in the W07 parameters across all GRB's.

### 3.2. Results from GP

The GP model captures the underlying trend of the LCs while also modeling the uncertainties introduced by the noise in the data.

Fig. 10, illustrates the reconstruction for each category, highlighting the accuracy of the GP model in recovering the main features of the LCs.

For the parameter  $\log(T_a)$ , we observe an average decrease in the error fraction of 22.27%. Similarly, for  $\log(F_a)$  and  $\alpha$  the average decreases in error fraction are 22.49% and 32.97%, respectively. Note that in this case, the error fractions are also calculated according to Eq. 18. The histogram distributions of Fig. 11 show the distribution of the relative percentage decrease of the three W07 parameters. The GP results for W07 are given for each GRB in Table 4.

### 3.3. Results from Long Short-Term Memory

For all categories of GRBs, we show the reconstructed LCs and compare the performance of the LSTM model with the original observed data. The LSTM model, being a deep learning technique, excels at learning temporal dependencies and making precise predictions, even when faced with noisy data.

Fig. 12 illustrates the reconstruction results for each category. The LSTM model demonstrates its ability to accurately capture trends in the LCs.

After reconstructing the LCs with the LSTM model, we use the W07 model to fit the reconstructed data. For the parameter  $\log(T_a)$ , the error fraction decreases by 29% on average. Similarly, for  $\log(F_a)$  and  $\alpha$ , the average decrease in error fraction is 31% and 40%, respectively. Note that the error fractions are calculated using Eq. 18. The histogram distributions in Fig. 13 illustrate the relative percentage decrease of the three W07 parameters. For each GRB, the GP results for W07 are provided in Table 5.

### 3.4. Results from CGAN

The CGAN model's generative approach effectively comprehends the actual signal's data distribution. The performance of the reconstructed data from CGAN is compared to the original observed data for all varieties of GRBs, as shown in Table 6. Reconstruction of a sample dataset for all four categories is shown in Fig. 15.

Once the LC reconstruction is done, the W07 model is applied, computing the decrease in error fraction as given by Eq. 18. Data reconstruction results in the decrease of the  $\log(F_a)$  error fraction by 23% and the  $\log(T_a)$  error fraction by 24%. The parameter  $\alpha$  also shows an average decrease of 31%. Fig. 14 shows the error fraction distribution plot for the CGAN model for three different W07 parameters.

### 3.5. Results from SARIMAX-Kalman Model

The SARIMAX-Kalman model was able to reconstruct the GRBs for all four categories. As observed, the model produced results even for noisy data. The mean reconstructed flux curve,  $\bar{F}_t$ , closely approximated the true flux values at all time points.

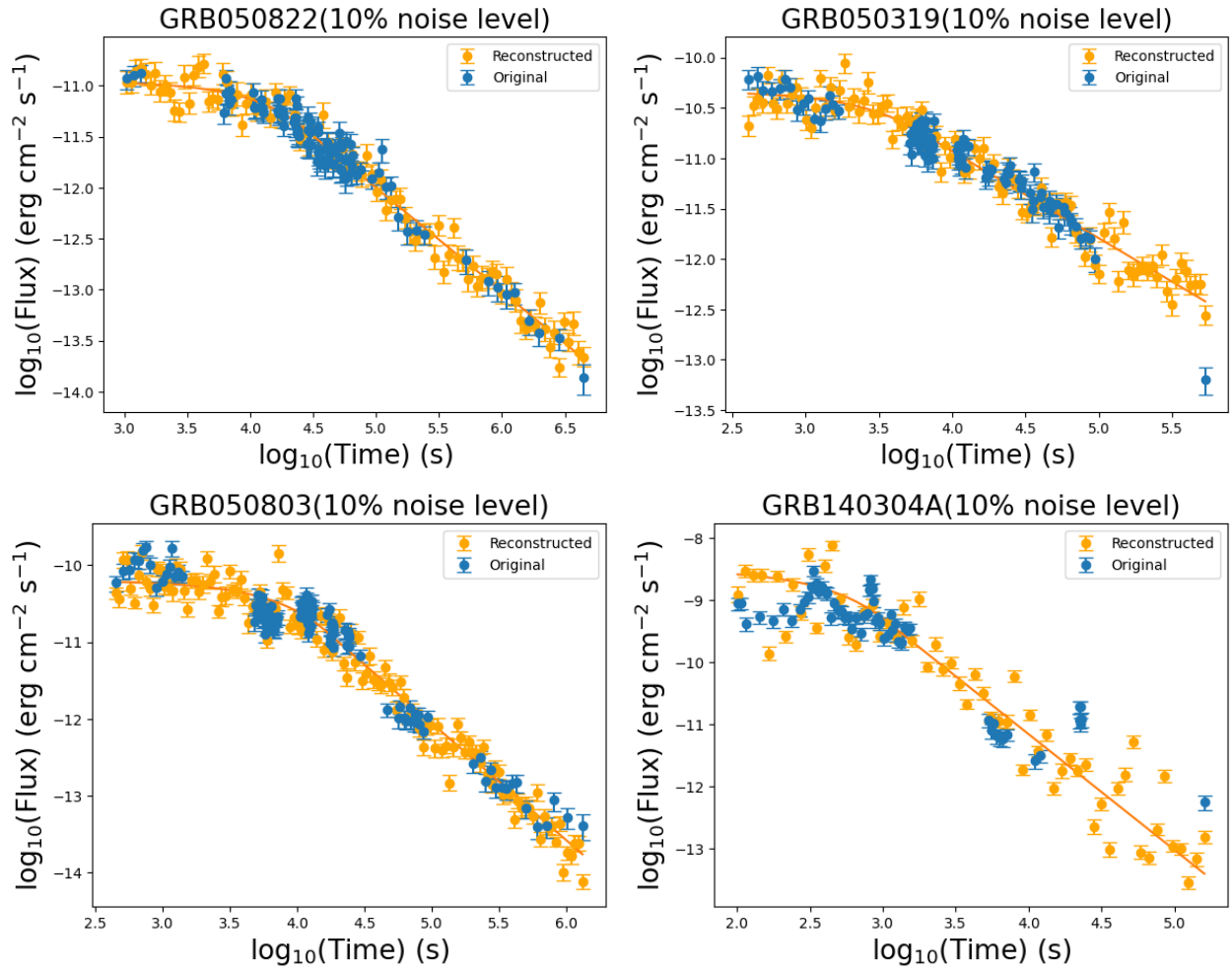


Figure 7: Reconstructed LCs after the W07 function at 10% noise level for all four classes: i) Good GRBs (upper left); ii) a break towards the end of the GRB LC (top right); iii) flares or Bumps in the afterglow (bottom left); iv) flares or Bumps with a Double Break towards the end of the GRB LC (bottom right).

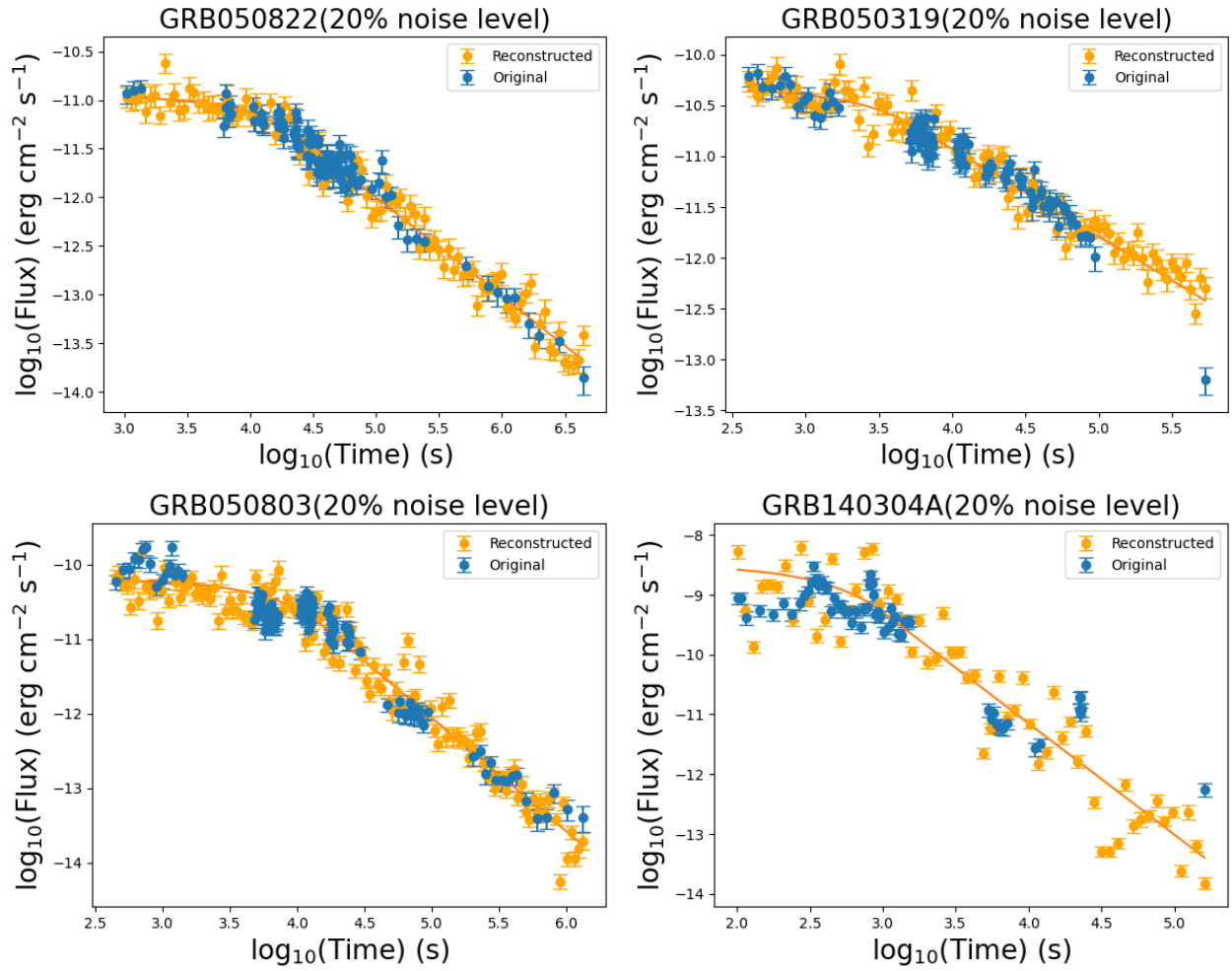


Figure 8: Reconstructed LCs with the W07 function method at 20% noise level for all four classes: i) Good GRBs (upper left); ii) a break towards the end of the GRB LC (upper right); iii) flares or bumps in the afterglow (bottom left); iv) flares or bumps with a double Break towards the end of the LC (bottom right).

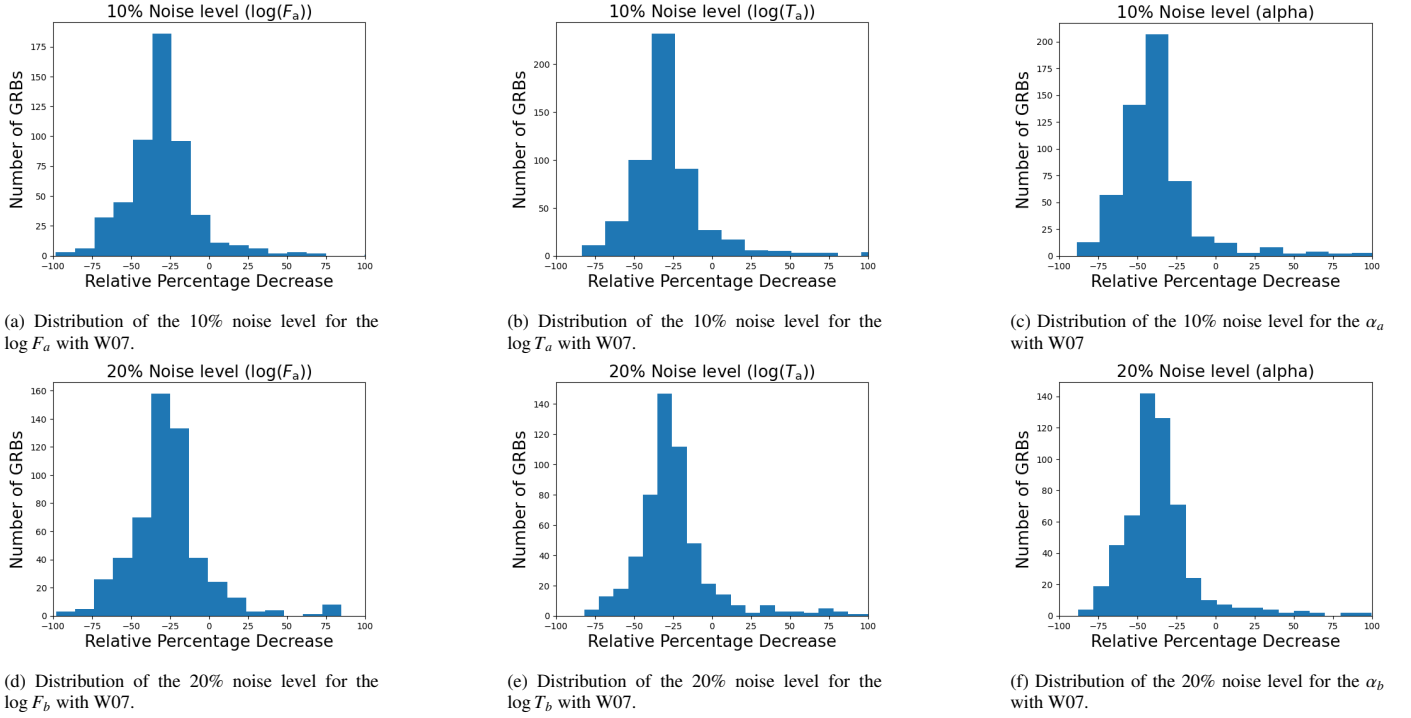


Figure 9: Distribution of Relative Percentage Decrease in the parameters of the W07 function following the application of the W07 for the reconstruction.

GRB ID	$EF_{\log_{10}(T_i)}$	$EF_{\log_{10}(F_i)}$	$EF_{\alpha_i}$	$EF_{\log_{10}(T_i)}$ RC	$EF_{\log_{10}(F_i)}$ RC	$EF_{\alpha_i}$ RC	% $\log_{10}(T_i)$	% $\log_{10}(F_i)$	% $\alpha_i$
050315	0.009277	0.002853	0.044366	0.009355	0.002182	0.029426	0.84	-23.5	-33.67
050318	0.010595	0.005542	0.045831	0.009678	0.005021	0.0436	-8.66	-9.39	-4.87
050319	0.016559	0.003891	0.040037	0.009885	0.002909	0.029084	-40.3	-25.23	-27.36
050401	0.009067	0.002015	0.026482	0.005214	0.001331	0.009225	-42.5	-33.96	-65.16
050416A	0.023629	0.004585	0.017749	0.020031	0.004262	0.012972	-15.23	-7.03	-26.92
050505	0.007041	0.002962	0.024572	0.004753	0.002165	0.013985	-32.49	-26.89	-43.09
050730	0.004394	0.002634	0.022533	0.002038	0.001214	0.006589	-53.62	-53.9	-70.76
050802	0.008957	0.002673	0.022622	0.006851	0.00228	0.01159	-23.51	-14.71	-48.77
050803	0.011301	0.004503	0.031987	0.009773	0.003585	0.021833	-13.52	-20.38	-31.74
050824	0.025016	0.005601	0.09427	0.015545	0.003848	0.062393	-37.86	-31.29	-33.81
050826	0.029099	0.018977	0.130694	0.019017	0.012187	0.164303	-34.65	-35.78	25.72
050904	0.021023	0.025741	0.188061	0.01269	0.008205	0.069846	-39.64	-68.13	-62.86
050915B	0.03593	0.008068	0.115451	0.027884	0.005908	0.080902	-22.39	-26.77	-29.93
050922C	0.01359	0.00337	0.010878	0.010991	0.002913	0.009379	-19.12	-13.57	-13.78
051016B	0.013664	0.003913	0.042293	0.00879	0.00246	0.023591	-35.67	-37.13	-44.22
051109A	0.011856	0.004577	0.015662	0.007808	0.002456	0.011811	-34.14	-46.34	-24.59
051109B	0.034645	0.007966	0.097658	0.027868	0.006029	0.054427	-19.56	-24.31	-44.27
051221A	0.020255	0.005388	0.050882	0.016785	0.004532	0.043126	-17.13	-15.89	-15.24
060124	0.008191	0.004158	0.011927	0.006046	0.003056	0.008663	-26.19	-26.5	-27.37
060206	0.018902	0.006636	0.024387	0.011812	0.003671	0.028674	-37.51	-44.67	17.58

Table 4: Similar content of Table 3, but using the GP reconstruction.

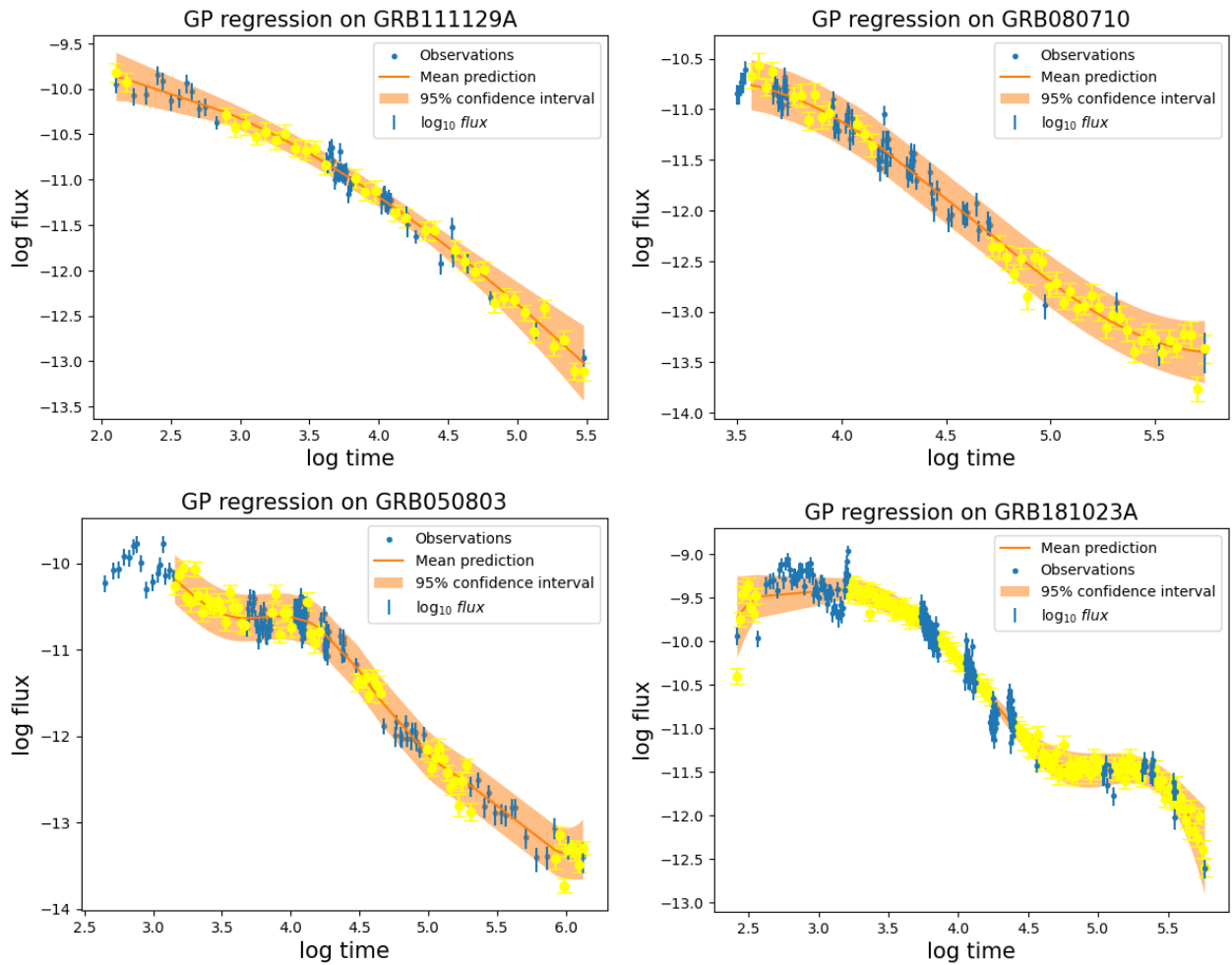


Figure 10: Reconstruction of LCs using GP for all 4 types of GRBs: i) Good GRBs (top left); ii) a GRB LC with a break towards the end (top right); iii) flares or bumps in the afterglow (bottom left); iv) flares or bumps with a double break towards the end of the LC (bottom right).

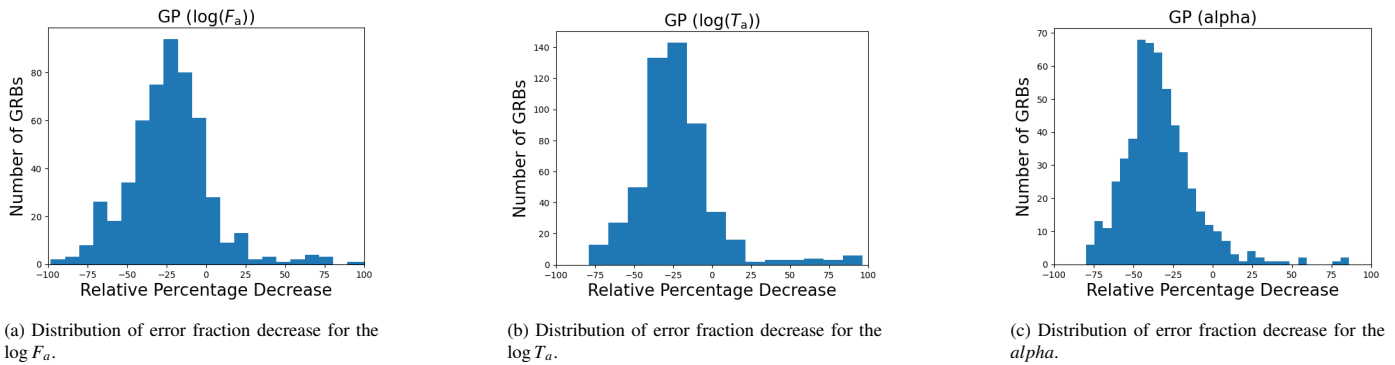


Figure 11: Distribution of Relative Percentage Decrease for the parameters of the W07 function following GP reconstruction.

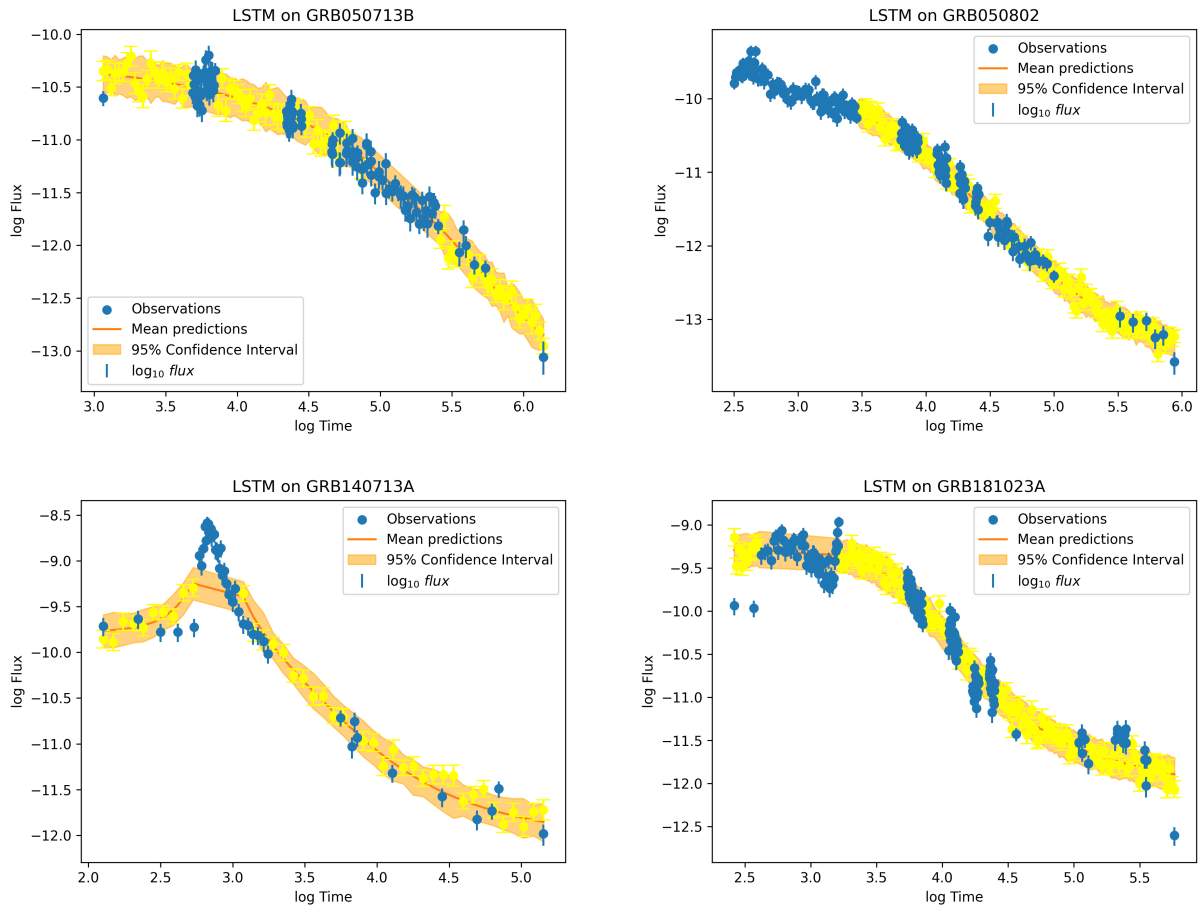


Figure 12: GRB LC reconstruction using LSTM model for all four types of GRBs: i) Good GRBs (top left); ii) a GRB LC with a break close to the end (top right); iii) flares or bumps in the afterglow (bottom left); and iv) flares or bumps with a double break close to the end of the LC (bottom right).

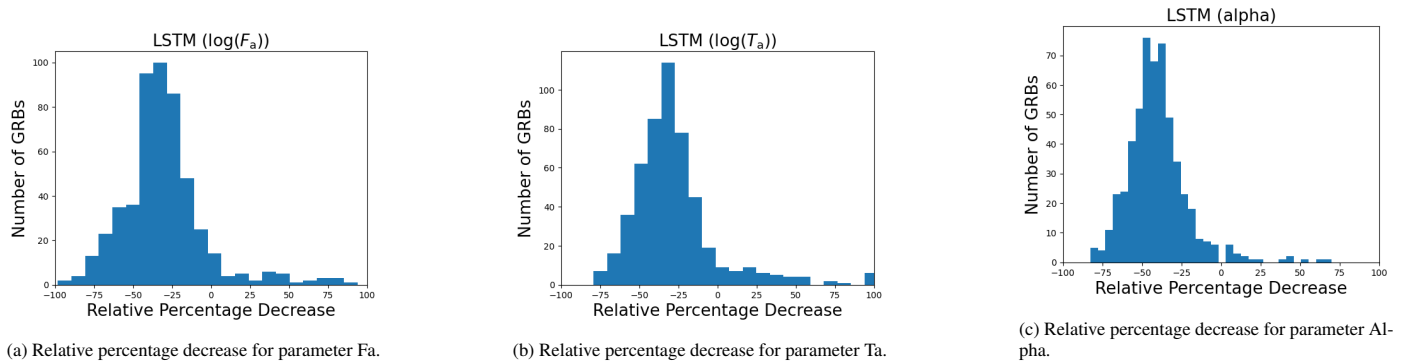


Figure 13: Distribution of Relative Percentage Decrease for the parameters of the W07 function following Bi-LSTM Reconstruction.



GRB ID	$EF_{\log_{10}(T_i)}$	$EF_{\log_{10}(F_i)}$	$EF_{\alpha_i}$	$EF_{\log_{10}(T_i)}$ RC	$EF_{\log_{10}(F_i)}$ RC	$EF_{\alpha_i}$ RC	$\% \log_{10}(T_i)$	$\% \log_{10}(F_i)$	$\% \alpha_i$
050315	0.0092	0.0028	0.0443	0.0074	0.0018	0.027	-20.06	-36.23	-36.91
050401	0.0090	0.0020	0.0264	0.0049	0.0012	0.0078	-45.7	-37.94	-70.35
070306	0.0058	0.0029	0.0325	0.0037	0.0016	0.0160	-35.39	-44.18	-50.61
070529	0.0219	0.0053	0.0288	0.0193	0.0049	0.0176	-12.02	-8.98	-38.83
080319B	0.0163	0.0080	0.0528	0.0118	0.0058	0.0345	-27.38	-26.81	-34.62
080928	0.0117	0.0057	0.0431	0.0090	0.0044	0.0192	-23.1	-23.49	-55.5
090423	0.0198	0.0075	0.0447	0.0147	0.0059	0.0221	-25.86	-21.71	-50.47
090426	0.0395	0.0081	0.0424	0.0256	0.0055	0.01873	-35.23	-31.76	-55.86
090510	0.0110	0.0041	0.0357	0.0103	0.0039	0.0287	-6.43	-6.14	-19.4
090519	0.0697	0.0179	0.2151	0.0341	0.0085	0.0920	-51.06	-52.61	-57.21
090529	0.0489	0.0094	0.1289	0.0584	0.0106	0.1010	19.44	11.97	-21.67
110818A	0.0155	0.0048	0.0490	0.0127	0.0043	0.0281	-17.56	-11.72	-42.74
111008A	0.0089	0.0026	0.0224	0.0064	0.0019	0.0136	-28.03	-27.52	-39.17
111123A	0.0159	0.0062	0.0721	0.0125	0.0048	0.0444	-21.34	-22.43	-38.36
111209A	0.0025	0.0023	0.0159	0.0029	0.0020	0.0051	18.42	-13.16	-67.66
171222A	0.0791	0.0173	0.1766	0.0322	0.0057	0.1305	-59.19	-66.6	-26.14
180205A	0.0276	0.0062	0.0383	0.0250	0.0060	0.0212	-9.35	-3.13	-44.71
180329B	0.0107	0.0043	0.0464	0.0074	0.0025	0.0221	-30.12	-41.04	-52.26
180404A	0.0295	0.0056	0.0873	0.0264	0.0048	0.0649	-10.37	-13.93	-25.67
190627A	0.0130	0.0054	0.0768	0.0079	0.0028	0.0392	-38.57	-46.79	-48.87

Table 5: Similar content of Table 3, but using the LSTM reconstruction.

GRB ID	$EF_{\log_{10}(T_i)}$	$EF_{\log_{10}(F_i)}$	$EF_{\alpha_i}$	$EF_{\log_{10}(T_i)}$ RC	$EF_{\log_{10}(F_i)}$ RC	$EF_{\alpha_i}$ RC	$\% \log_{10}(T_i)$	$\% \log_{10}(F_i)$	$\% \alpha_i$
050712	0.018	0.005	0.044	0.014	0.004	0.033	-20.08	-13.21	-23.3
050318	0.010	0.005	0.045	0.009	0.004	0.037	-8.97	-10.87	-17.34
050416A	0.023	0.004	0.017	0.016	0.003	0.013	-30.98	-34.2	-23.1
050607	0.021	0.005	0.044	0.020	0.005	0.035	-1.59	-2.46	-18.78
050713A	0.010	0.002	0.017	0.008	0.002	0.011	-13.82	-9.83	-35.29
050822	0.010	0.003	0.025	0.008	0.002	0.015	-25.1	-28.97	-40.38
050824	0.025	0.005	0.094	0.019	0.004	0.052	-23.54	-25.3	-44.28
050826	0.029	0.019	0.130	0.019	0.010	0.133	-31.49	-45.67	1.84
050915B	0.035	0.008	0.115	0.022	0.004	0.069	-37.82	-39.74	-40.04
051016A	0.032	0.005	0.050	0.018	0.003	0.022	-43.23	-34.19	-55.42
051109A	0.011	0.004	0.015	0.006	0.002	0.009	-42.61	-47.94	-36.94
051221A	0.020	0.005	0.050	0.015	0.003	0.036	-23.1	-27.02	-28.44
060105	0.003	0.001	0.007	0.003	0.001	0.003	-8.69	0.54	-47.4
060108	0.023	0.006	0.071	0.018	0.004	0.052	-21.78	-27.78	-26.64
060109	0.013	0.005	0.056	0.009	0.003	0.033	-29.83	-31.92	-40.19
060124	0.008	0.004	0.011	0.005	0.002	0.007	-31.11	-30.56	-37.81
060218	0.027	0.013	0.082	0.013	0.005	0.070	-49.97	-61.05	-13.71
060306	0.012	0.003	0.024	0.012	0.003	0.022	2.57	-7.53	-4.78
060418	0.018	0.005	0.030	0.011	0.003	0.011	-37.92	-24.84	-62.46
060421	0.040	0.010	0.086	0.063	0.014	0.059	54.57	43.54	-31.95

Table 6: Similar content of Table 3, but using the CGAN reconstruction.

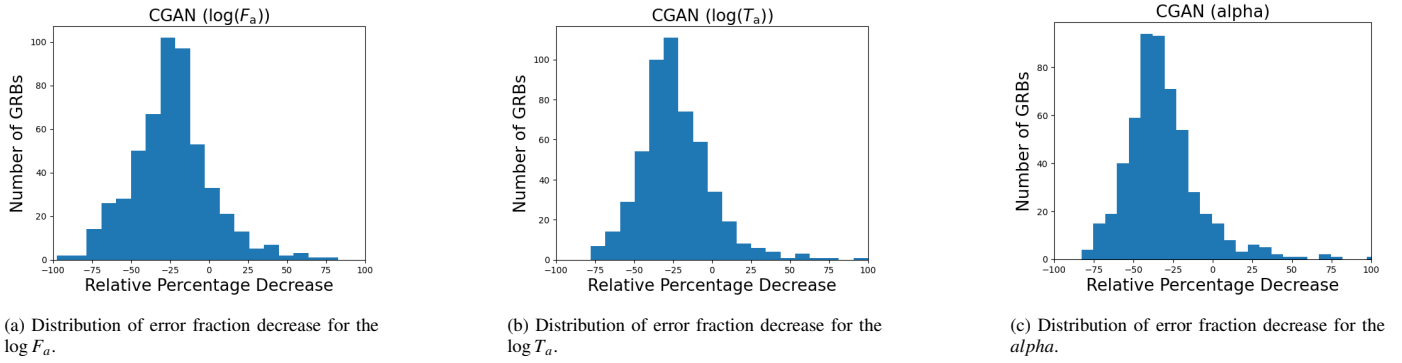


Figure 14: Distribution of Relative Percentage Decrease for the parameters of the W07 function after reconstruction using CGAN model.

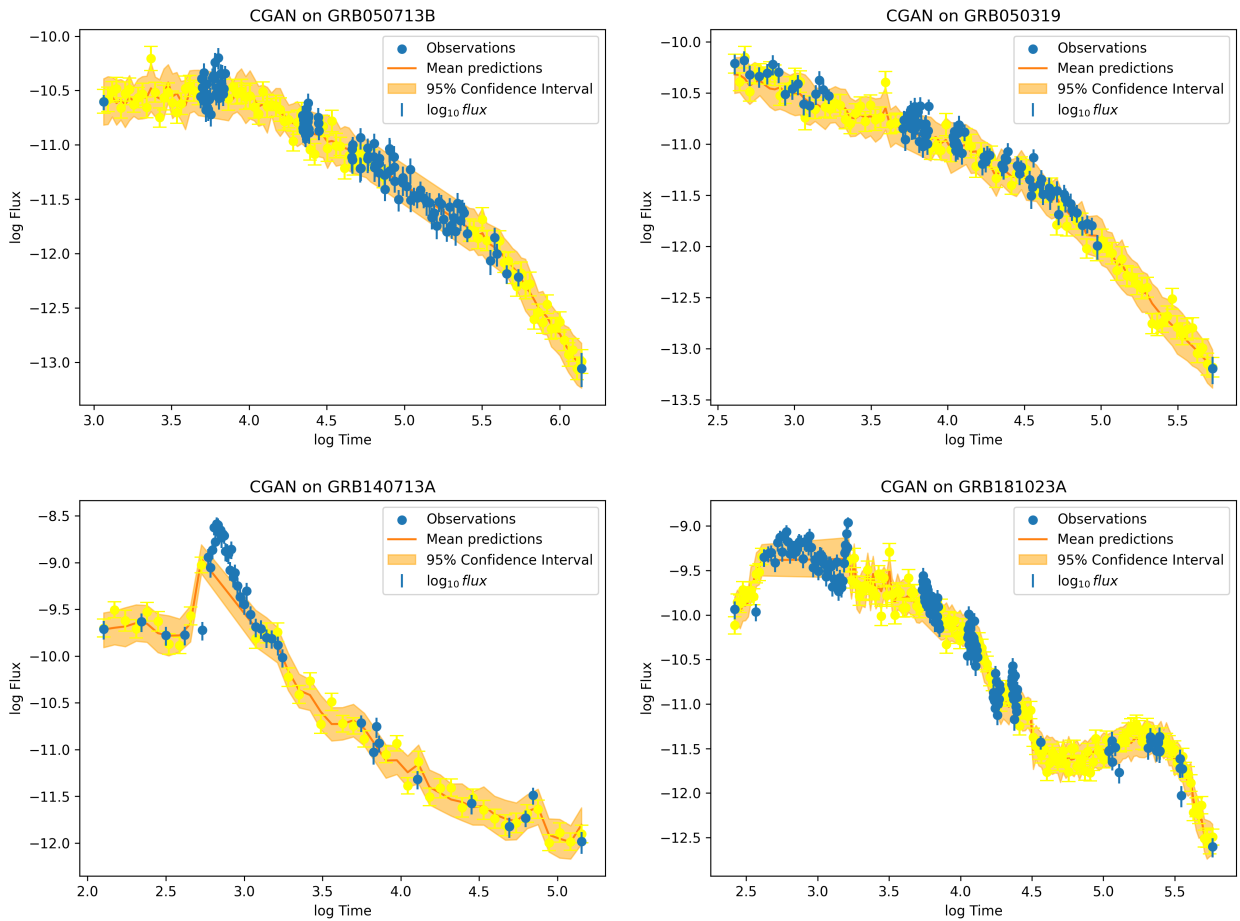


Figure 15: Reconstruction of GRB LC using CGAN model for all 4 types of GRBs: i) Good GRBs (top left); ii) A GRB LC with a break towards the end (top right); iii) flares or bumps in the afterglow (bottom left); iv) flares or bumps with a double break towards the end of the LC (bottom right).

GRB ID	$EF_{\log_{10}(T_i)}$	$EF_{\log_{10}(F_i)}$	$EF_{\alpha_i}$	$EF_{\log_{10}(T_i)}$ RC	$EF_{\log_{10}(F_i)}$ RC	$EF_{\alpha_i}$ RC	% $\log_{10}(T_i)$	% $\log_{10}(F_i)$	% $\alpha_i$
050319	0.01659	0.003891	0.040037	0.014382	0.003443	0.038019	-13.15	-11.52	-5.04
050505	0.007041	0.002962	0.024572	0.006667	0.002729	0.018767	-5.31	-7.86	-23.62
050824	0.025016	0.005601	0.09427	0.020188	0.00467	0.073656	-19.3	-16.63	-21.87
050904	0.021023	0.025741	0.188061	0.010668	0.007366	0.054765	-49.25	-71.38	-70.88
060218	0.027706	0.01355	0.082089	0.019851	0.008152	0.127561	-28.35	-39.84	55.39
060418	0.018354	0.005008	0.030277	0.012832	0.004885	0.014731	-30.09	-2.45	-51.34
060607A	0.005907	0.006904	0.047534	0.005094	0.003896	0.023927	-13.77	-43.57	-49.66
070802	0.060238	0.014903	0.179529	0.048351	0.00994	0.100446	-19.73	-33.3	-44.05
071003	0.02059	0.011638	0.092524	0.015357	0.008643	0.051068	-25.42	-25.73	-44.8
081029	0.009562	0.007018	0.067153	0.007542	0.004184	0.03031	-21.12	-40.38	-54.86
081203A	0.009779	0.005213	0.034454	0.009045	0.004853	0.024376	-7.51	-6.91	-29.25
090809	0.052156	0.028509	0.195152	0.024973	0.012906	0.137961	-52.12	-54.73	-29.31
100625A	0.098176	0.03324	0.131585	0.037082	0.012416	0.053535	-62.23	-62.65	-59.32
100906A	0.010133	0.004656	0.034657	0.008552	0.003477	0.026793	-15.61	-25.3	-22.69
120404A	0.017972	0.010615	0.063669	0.014378	0.005397	0.040925	-20	-49.15	-35.72
111008A	0.008942	0.002673	0.022496	0.008691	0.002155	0.019879	-2.8	-19.36	-11.63
130418A	0.026513	0.006539	0.024621	0.012192	0.003771	0.012428	-54.02	-42.33	-49.52
140614A	0.026741	0.010302	0.068694	0.023282	0.007749	0.066152	-12.94	-24.78	-3.7
151021A	0.016493	0.006515	0.016056	0.014172	0.004323	0.015591	-14.08	-33.64	-2.9
210210A	0.027058	0.006826	0.076937	0.015788	0.004068	0.034798	-41.65	-40.4	-54.77

Table 7: Similar content of Table 3, but using the SARIMAX+Kalman.

Fig. 17 shows the LCs reconstructed using the SARIMAX-Kalman model for all categories of GRB. The performance of the reconstruction using SARIMAX+Kalman compared to the original observed data for all varieties of GRBs is as shown in Table 7.

For the parameters  $\log(T_a)$  and  $\log(F_a)$ , an average decrease in error fraction of 5% and 14% is observed, respectively. The average decrease in error fraction for  $\alpha$  is 6%, and the distribution plots for the relative percentage decrease for the three W07 parameters are shown in Fig. 16. The error fractions are calculated according to Eq. 18.

The average percentage decrease for all models in the uncertainties of the parameters for all GRBs is given in Table 8.

Reconstruction Process	% avg $\log_{10}(T_a)$	% avg $\log_{10}(F_a)$	% avg alpha
W07 reconstruction (10%)	-24.5	-25.7	-36.17
W07 reconstruction (20%)	-21.2	-22.98	-34.72
GP	-22.27	-22.49	-32.97
Bi-LSTM	-28.64	-30.74	-40.18
CGAN	-23.47	-23.81	-31.2
Sarimax-based Kalman	-13.5	-5.29	-5.5

Table 8: Overview of average percentage decrease in uncertainty for across reconstruction processes and parameters.

#### 4. Summary and Conclusion

We present the reconstruction of 545 GRB using three new models compared to published papers in the GRB field: Bi-LSTM, CGAN, and the Sarimax-based Kalman method. Furthermore, we included the reconstruction using the W07 model and GP for comparison, extending the analysis of the previous

work of Dainotti et al. 2023b by applying it to the four GRB classifications defined in this study. We demonstrated the effectiveness of the approaches in reconstructing LCs and addressing temporal gaps in GRB observations. Here, we highlight the main points of our results:

- Upon re-fitting the reconstructed LCs with the W07 model, we found:
  - At the 10% noise level, the error fractions have decreased by 25% for  $\log T_a$ , 26% for  $\log F_a$  and 36% for  $\alpha$ .
  - At the 20% noise level, these reductions were slightly lower, as expected, with decreases of 21% for  $\log T_a$ , 23% for  $\log F_a$  and 35% for  $\alpha$ .
- The LSTM model demonstrated the most significant improvements, with average reductions in error fractions of 29% for  $\log T_a$ , 31% for  $\log F_a$  and 40% for  $\alpha$ . This performance highlights the model’s ability to capture long-range dependencies in the data, making it particularly effective for reconstructing more complex LC features such as flares and breaks.
- GP also performed consistently well, achieving average reductions of 22% for both  $\log T_a$  and  $\log F_a$  and 33% for  $\alpha$ .
- The CGAN model showed slightly less pronounced improvements, with decreases of 23% in  $\log T_a$ , 24% in  $\log F_a$  and 31% for  $\alpha$ .
- The Sarimax-based Kalman method demonstrated effectiveness for well-sampled GRBs, as the model showed

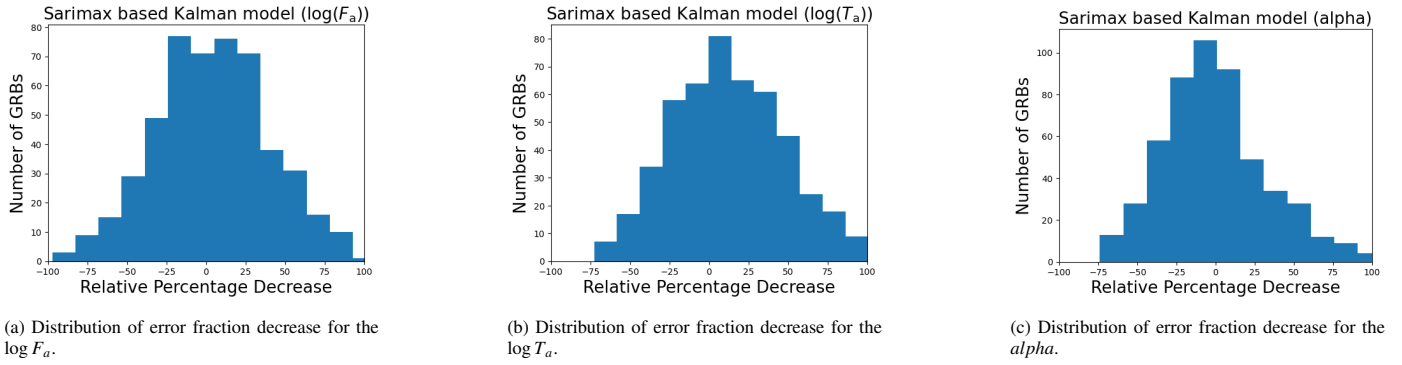


Figure 16: Distribution of Relative Percentage Decrease for the parameters of the W07 function following reconstruction of LCs using SARIMA-Kalman model.

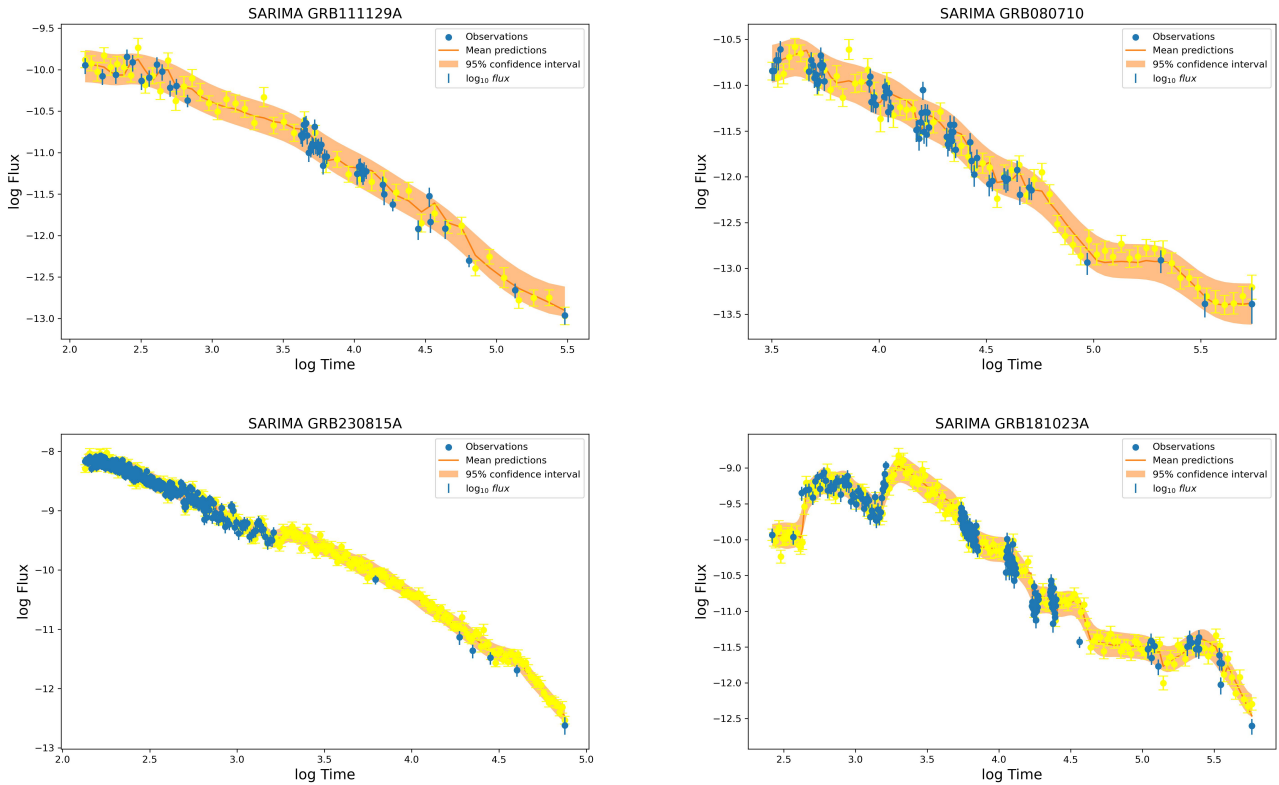


Figure 17: Reconstruction of GRB LC using SARIMA-Kalman model for all 4 types of GRBs: i) Good GRBs (upper left); ii) GRB LCs with a break towards the end. (top right); iii) flares or bumps in the afterglow (bottom left); iv) flares or bumps with a double break towards the end of the LC (bottom right).

more modest reductions in error fractions, with decreases of 5% for  $\log T_a$ , 14% for  $\log F_a$  and 6% for  $\alpha$ , particularly having issues with more complex features such as flares and multiple breaks.

- A comparison of the relative percentage changes highlights that while the LSTM model consistently achieves the highest uncertainty reductions across all parameters, the GP and CGAN models perform approximately 10% less effectively in terms of these uncertainty reductions. In contrast, the Sarimax-based Kalman model has uncertainty reductions approximately 15% lower than LSTM, particularly with complex LCs.
- In general, the LSTM model proved to be the most effective approach to reconstruct the LC of GRB, especially for complex scenarios.

A comparison with previous studies (Dainotti et al., 2023b; Sourav et al., 2023) shows:

- Dainotti et al. 2023b performed the analysis on a sample of 218 Good GRBs and shows an average reduction of 37% for all parameters at the 10% noise level and 34% at the 20% noise level using the W07 model. For the GP model, an average reduction of 31% was observed.
- In contrast, the current study observed lower reductions due to a more diverse sample of 545 GRBs, including the four classifications (Good, breaks, flares, and complex features), which introduces more variability and complexity in the reconstruction process. Furthermore, we performed the analysis on a subset of 299 Good GRBs, for which the LSTM model demonstrated a reduction of approximately 40%, which is significantly more performant (8 % increase) than 37% of the reduction in uncertainties reported in Dainotti et al. 2023b.
- Compared to Sourav et al. 2023, our Bi-LSTM model performs better by achieving a 29% reduction in uncertainty for the parameter  $\log F_a$ , while Sourav et al. 2023 achieves a 24% reduction in uncertainty for  $\log F_a$  throughout the sample that contains all four classes of GRBs. It is worth noting that we have performed the calculation in all the parameter space, while Sourav et al. 2023 only for the flux values.

The significant reduction in uncertainties achieved through these reconstructions enhances the reliability of the GRB plateau parameters, because with their reduced uncertainties, the relations involving the plateau emission can be used as standard cosmological candles (Dainotti et al., 2022g; Dainotti et al., 2022c, 2023a).

In a follow-up manuscript, we will explore advanced deep-learning architectures such as CNN-based autoencoders, multilayer perceptrons, genetic algorithms, and recurrent neural networks. Additionally, transformer-based and large language models will be investigated for their ability to capture intricate

temporal dependencies. These methods, coupled with emerging datasets, hold great potential for further improving the precision, reliability, and applicability of LC reconstruction in the field of theoretical model interpretation and for cosmology. Importantly, this reconstruction has been built entirely on the Swift LCs, but our plan is to extend to other current SVOM Atteia et al. 2022, Einstein Probe Yuan et al. 2022 or future missions, such as THESEUS Amati et al. 2018 and HiZ-GUNDAM Yonetoku et al. 2024 and across different wavelengths as well. The extension of this work to optical wavelengths will be timely, especially in view of the largest optical catalog to date (Dainotti et al., 2020a, 2022b, 2024a,b; Zhang and Mészáros, 2004).

## 5. Appendix

Here we present three additional models that we had tried but did not yield a promising prediction. We do not exclude that these models with different hybrid combinations can have larger potential with future attempts.

### 5.1. Decision Trees

Decision Trees (DTs) are a non-parametric supervised learning method mainly used for classification and regression. We use the CART algorithm, which stands for Classification and Regression Tree algorithm, to build a tree and the Python package scikit-learn for implementing Decision Trees for Regression.

They work by recursively splitting the data based on feature values, aiming to minimize the variance within the resulting subgroups. For LCR, decision trees are particularly useful because they handle nonlinear relationships well. However, decision trees tend to overfit the training data, especially when the LC has noisy measurements or complex temporal behavior. Although they perform well in capturing local variations, their predictions often lack the smoothness required for continuous processes like LCR. This limitation leads to step-like predictions rather than a smooth, gradual transition typically expected in astronomical LCs.

One major drawback is their inability to provide uncertainty estimates. Unlike probabilistic models, decision trees output point estimates without any measure of confidence, making them less suitable for tasks where understanding the uncertainty is critical.

### 5.2. Random Forest

Random Forests are an ensemble method that builds upon the foundation of decision trees by creating multiple trees using random subsets of the data and features and then averaging their predictions. This ensemble approach helps mitigate the overfitting issue commonly seen in single decision trees, leading to improved performance.

One significant advantage Random Forests have over individual decision trees is their ability to estimate uncertainty. Although Random Forests are not inherently probabilistic models,

uncertainty can be estimated by measuring the variance of predictions across the ensemble of trees. By examining the distribution of predictions from the individual trees, Random Forests provide a form of uncertainty quantification.

However, while Random Forests offer some level of uncertainty estimation, they are still less precise than the uncertainty provided by fully probabilistic models like GPs. Random Forest uncertainty is derived from the diversity among trees rather than the underlying data noise or model uncertainty, and the predicted intervals are less smooth and more step-like compared to probabilistic methods as shown in Fig. 18.

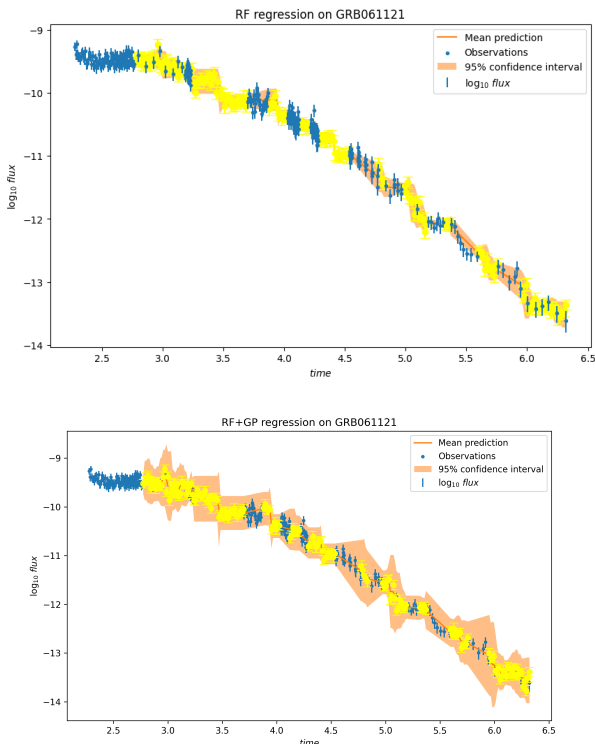


Figure 18: Reconstructed GRB LCs using i) Random Forest model (left); ii) Incorporation of both Random Forest and GP Regression Models (right).

### 5.3. The Hybrid Model: Random Forest with Gaussian Process

To counter the step-like nature of Random Forest predictions in LCR, we develop a hybrid model by combining Random Forest with a GP. Here, the Random Forest acts as the base model, trained on the data to capture initial predictions that efficiently handle nonlinear relationships. However, due to the Random Forest’s step-like nature, these predictions lack the smoothness typically required for reconstructing continuous time-series data.

Once the Random Forest produces its predictions, they are passed to a GP for further modeling. The GP is trained on the Random Forest predictions, learning a functional mapping that transforms the step-like predictions into smoother, continuous outputs. GPs are particularly well-suited for this task due to their ability to model uncertainty in a probabilistic framework while naturally producing smooth, continuous predictions. By

integrating the GP, we aim to refine the overall prediction, achieving a smoother representation of the LC with a continuity that better reflects its underlying structure.

However, a limitation of this approach is that the error propagation from the Random Forest propagates through to the GP, and the step-like uncertainty patterns remain prominent in the hybrid model’s confidence intervals. While the mean predictions become smoother, the uncertainty estimates retain a step-like nature as shown in Figure 3. Thus, this hybrid model improves the smoothness of the LC reconstruction, but still lacks the fully continuous uncertainty representation characteristic of models with an entirely probabilistic approach.

## Acknowledgements

We thank Biagio De Simone for the initial code for the reconstruction of LCs. We thank Prof Dieter Hartmann, Aditya Narendra, Dhruv Bal and Nikita Khatiya for their insightful remarks and invaluable assistance in commenting on the analysis of our models. We thank Federico Da Rold and Spencer James Gibson for their valuable suggestions regarding the exploration of different new algorithms for the reconstruction process.

We thank Dr. Konstantinos F. Dialektopoulos, Dr. Jurgen Mifsud, Prof. Jackson Said and Dr. Purba Mukherjee for their helpful comments and discussion of our analysis. We also thank Aditi Sant, Adrija Saha, Syed Naqi, and Shri Prathaa for their help in the analysis.

## References

- Ahumada, T., Singer, L.P., Anand, S., Coughlin, M.W., Kasliwal, M.M., Ryan, G., Andreoni, I., Cenko, S.B., Fremling, C., Kumar, H., Pang, P.T.H., Burns, E., Cunningham, V., Dichiaro, S., Dietrich, T., Svinkin, D.S., Almualla, M., Castro-Tirado, A.J., De, K., Dunwoody, R., Gatkine, P., Hammerstein, E., Iyyani, S., Mangan, J., Perley, D., Purkayastha, S., Bellm, E., Bhalerao, V., Bolin, B., Bulla, M., Cannella, C., Chandra, P., Duev, D.A., Frederiks, D., Gal-Yam, A., Graham, M., Ho, A.Y.Q., Hurley, K., Karambelkar, V., Kool, E.C., Kulkarni, S.R., Mahabal, A., Masci, F., McBreen, S., Pandey, S.B., Reusch, S., Ridnaia, A., Rosnet, P., Rusholme, B., Carracedo, A.S., Smith, R., Soumagnac, M., Stein, R., Troja, E., Tsvetkova, A., Walters, R., Valeev, A.F., 2021. Discovery and confirmation of the shortest gamma-ray burst from a collapsar. *Nature Astronomy* 5, 917–927. doi:10.1038/s41550-021-01428-7, arXiv:2105.05067.
- Akiba, T., Sano, S., Yanase, T., Ohta, T., Koyama, M., 2019. Optuna: A next-generation hyperparameter optimization framework, in: Proceedings of the 25th ACM SIGKDD international conference on knowledge discovery & data mining, pp. 2623–2631.
- Aloy, M.Á., Obergaulinger, M., 2021. Magnetorotational core collapse of possible GRB progenitors - II. Formation of protomagnetars and collapsars. *Monthly Notices of the Royal Astronomical Society* 500, 4365–4397. doi:10.1093/mnras/staa3273, arXiv:2008.03779.
- Amati, L., O’Brien, P., Götz, D., Bozzo, E., Tenzer, C., Frontera, F., Ghirlanda, G., Labanti, C., Osborne, J., Stratta, G., et al., 2018. The theses space mission concept: science case, design and expected performances. *Advances in Space Research* 62, 191–244.
- Atteia, J.L., Cordier, B., Wei, J., 2022. The svom mission. *International Journal of Modern Physics D* 31, 2230008.
- Barthelmy, S.D., Barbier, L.M., Cummings, J.R., Fenimore, E.E., Gehrels, N., Hullinger, D., Krimm, H.A., Markwardt, C.B., Palmer, D.M., Parsons, A., Sato, G., Suzuki, M., Takahashi, T., Tashiro, M., Tueller, J., 2005. The Burst Alert Telescope (BAT) on the SWIFT Midex Mission. *Space Science Reviews* 120, 143–164. doi:10.1007/s11214-005-5096-3, arXiv:astro-ph/0507410.

Beskin, G., Karpov, S., Bondar, S., Greco, G., Guarnieri, A., Bartolini, C., Piccioni, A., 2010. Fast Optical Variability of a Naked-eye Burst—Manifestation of the Periodic Activity of an Internal Engine. *The Astrophysical Journal Letters* 719, L10–L14. doi:10.1088/2041-8205/719/1/L10, arXiv:0905.4431.

Betoule, M., Kessler, R., Guy, J., Mosser, J., Hardin, D., Biswas, R., Astier, P., El-Hage, P., Konig, M., Kuhlmann, S., Marriner, J., Pain, R., Regnault, N., Balland, C., Bassett, B.A., Brown, P.J., Campbell, H., Carlberg, R.G., Cellier-Holzem, F., Cinabro, D., Conley, A., D’Andrea, C.B., DePoy, D.L., Doi, M., Ellis, R.S., Fabbro, S., Filippenko, A.V., Foley, R.J., Frieman, J.A., Fouchez, D., Galbany, L., Goobar, A., Gupta, R.R., Hill, G.J., Hlozek, R., Hogan, C.J., Hook, I.M., Howell, D.A., Jha, S.W., Le Guillou, L., Leloudas, G., Lidman, C., Marshall, J.L., Möller, A., Mourão, A.M., Neveu, J., Nichol, R., Olmstead, M.D., Palanque-Delabrouille, N., Perlmutter, S., Prieto, J.L., Pritchett, C.J., Richmond, M., Riess, A.G., Ruhlmann-Kleider, V., Sako, M., Schahmanche, K., Schneider, D.P., Smith, M., Sollerman, J., Sullivan, M., Walton, N.A., Wheeler, C.J., 2014. Improved cosmological constraints from a joint analysis of the sdss-ii and snls supernova samples. *Astronomy & Astrophysics*.

Bi, X., Mao, J., Liu, C., Bai, J.M., 2018. Statistical Study of the Swift X-Ray Flash and X-Ray Rich Gamma-Ray Bursts. *The Astrophysical Journal* 866, 97. doi:10.3847/1538-4357/aadcf8, arXiv:1810.03079.

Blake, C.H., Bloom, J.S., Starr, D.L., Falco, E.E., Skrutskie, M., Fenimore, E.E., Duchêne, G., Szentgyorgyi, A., Hornstein, S., Prochaska, J.X., McCabe, C., Ghez, A., Konopacky, Q., Stapelfeldt, K., Hurley, K., Campbell, R., Kassis, M., Chaffee, F., Gehrels, N., Barthelmy, S., Cummings, J.R., Hullinger, D., Krimm, H.A., Markwardt, C.B., Palmer, D., Parsons, A., McLean, K., Tueller, J., 2005. An infrared flash contemporaneous with the  $\gamma$ -rays of GRB 041219a. *Nature* 435, 181–184. doi:10.1038/nature03520, arXiv:astro-ph/0503508.

Bloom, J.S., Kulkarni, S.R., Djorgovski, S.G., 2002. The Observed Offset Distribution of Gamma-Ray Bursts from Their Host Galaxies: A Robust Clue to the Nature of the Progenitors. *The Astronomical Journal* 123, 1111–1148. doi:10.1086/338893, arXiv:astro-ph/0010176.

Bucciantini, N., Metzger, B.D., Thompson, T.A., Quataert, E., 2012. Short gamma-ray bursts with extended emission from magnetar birth: jet formation and collimation. *Monthly Notices of the Royal Astronomical Society* 419, 1537–1545. doi:10.1111/j.1365-2966.2011.19810.x, arXiv:1106.4668.

Bucciantini, N., Quataert, E., Arons, J., Metzger, B.D., Thompson, T.A., 2008. Relativistic jets and long-duration gamma-ray bursts from the birth of magnetars. *Monthly Notices of the Royal Astronomical Society* 383, L25–L29. doi:10.1111/j.1745-3933.2007.00403.x, arXiv:0707.2100.

Burrows, D.N., Hill, J.E., Nousek, J.A., Kennea, J.A., Wells, A., Osborne, J.P., Abbey, A.F., Beardmore, A., Mukerjee, K., Short, A.D.T., Chincarini, G., Campana, S., Citterio, O., Moretti, A., Pagani, C., Tagliaferri, G., Giommi, P., Capalbi, M., Tamburelli, F., Angelini, L., Cusumano, G., Bräuninger, H.W., Burkert, W., Hartner, G.D., 2005. The Swift X-Ray Telescope. *Space Science Reviews* 120, 165–195. doi:10.1007/s11214-005-5097-2, arXiv:astro-ph/0508071.

Cano, Z., Wang, S.Q., Dai, Z.G., Wu, X.F., 2017. The Observer’s Guide to the Gamma-Ray Burst Supernova Connection. *Advances in Astronomy* 2017, 8929054. doi:10.1155/2017/8929054, arXiv:1604.03549.

Cao, S., Dainotti, M., Ratra, B., 2022a. Standardizing Platinum Dainotti-correlated gamma-ray bursts, and using them with standardized Amati-correlated gamma-ray bursts to constrain cosmological model parameters. *Monthly Notices of the Royal Astronomical Society* 512, 439–454. doi:10.1093/mnras/stac517, arXiv:2201.05245.

Cao, S., Khadka, N., Ratra, B., 2022b. Standardizing Dainotti-correlated gamma-ray bursts, and using them with standardized Amati-correlated gamma-ray bursts to constrain cosmological model parameters. *Monthly Notices of the Royal Astronomical Society* 510, 2928–2947. doi:10.1093/mnras/stab3559, arXiv:2110.14840.

Cardone, V.F., Capozziello, S., Dainotti, M.G., 2009. An updated gamma-ray bursts hubble diagram. *Monthly Notices of the Royal Astronomical Society* 400, 775–790. doi:10.1111/j.1365-2966.2009.15456.x.

Cardone, V.F., Dainotti, M.G., Capozziello, S., Willingale, R., 2010. Constraining cosmological parameters by gamma-ray burst x-ray afterglow light curves. *Monthly Notices of the Royal Astronomical Society* 408, 1181–1186. doi:10.1111/j.1365-2966.2010.17197.x.

Costa, E., Frontera, F., Heise, J., Feroci, M., in’t Zand, J., Fiore, F., Cinti, M.N., Dal Fiume, D., Nicastro, L., Orlandini, M., Palazzi, E., Rapisarda#, M., Zavattini, G., Jager, R., Parmar, A., Owens, A., Molendi, S., Cusumano, G., Maccarone, M.C., Giarrusso, S., Coletta, A., Antonelli, L.A., Giommi, P., Muller, J.M., Piro, L., Butler, R.C., 1997. Discovery of an X-ray afterglow associated with the  $\gamma$ -ray burst of 28 February 1997. *Nature* 387, 783–785. doi:10.1038/42885, arXiv:astro-ph/9706065.

Cucchiara, A., Levan, A.J., Fox, D.B., Tanvir, N.R., Ukwatta, T.N., Berger, E., Krühler, T., Küpcü Yoldaş, A., Wu, X.F., Toma, K., Greiner, J., Olivares, F.E., Rowlinson, A., Amati, L., Sakamoto, T., Roth, K., Stephens, A., Fritz, A., Fynbo, J.P.U., Hjorth, J., Malesani, D., Jakobsson, P., Wiersema, K., O’Brien, P.T., Soderberg, A.M., Foley, R.J., Fruchter, A.S., Rhoads, J., Rutledge, R.E., Schmidt, B.P., Dopita, M.A., Podsiadlowski, P., Willingale, R., Wolf, C., Kulkarni, S.R., D’Avanzo, P., 2011. A Photometric Redshift of  $z \sim 9.4$  for GRB 090429B. *The Astrophysical Journal* 736, 7. doi:10.1088/0004-637X/736/1/7, arXiv:1105.4915.

Dainotti, M., Bhardwaj, S., Bissaldi, E., Fraija, N., Sourav, S., Galvan-Gamez, A., 2024a. Analysis of grb closure relationship in multi-wavelengths. arXiv preprint arXiv:2411.10736.

Dainotti, M., De Simone, B., Mohideen Malik, R., Pasumarti, V., Levine, D., Saha, N., Gendre, B., Kido, D., Watson, A., Becerra, R., et al., 2024b. An optical gamma-ray burst catalogue with measured redshift–i. data release of 535 gamma-ray bursts and colour evolution. *Monthly Notices of the Royal Astronomical Society* 533, 4023–4043.

Dainotti, M., Lenart, A.Ł., Chraya, A., Sarracino, G., Nagataki, S., Fraija, N., Capozziello, S., Bogdan, M., 2023a. The gamma-ray bursts fundamental plane correlation as a cosmological tool. *Monthly Notices of the Royal Astronomical Society* 518, 2201–2240.

Dainotti, M., Livermore, S., Kann, D., Li, L., Oates, S., Yi, S., Zhang, B., Gendre, B., Cenko, B., Fraija, N., 2020a. The optical luminosity–time correlation for more than 100 gamma-ray burst afterglows. *The Astrophysical Journal Letters* 905, L26.

Dainotti, M., Taira, E., Wang, E., Lehman, E., Narendra, A., Pollo, A., Madejski, G.M., Petrosian, V., Bogdan, M., Dey, A., et al., 2024c. Inferring the redshift of more than 150 grbs with a machine learning ensemble model. arXiv preprint arXiv:2401.03589.

Dainotti, M.G., Cardone, V.F., Capozziello, S., 2008. A time-luminosity correlation for  $\gamma$ -ray bursts in the X-rays. *Monthly Notices of the Royal Astronomical Society* 391, L79–L83. doi:10.1111/j.1745-3933.2008.00560.x, arXiv:0809.1389.

Dainotti, M.G., De Simone, B., Islam, K.M., Kawaguchi, K., Moriya, T.J., Takiwaki, T., Tominaga, N., Gangopadhyay, A., 2022a. The Quest for New Correlations in the Realm of the Gamma-Ray Burst-Supernova Connection. *The Astrophysical Journal* 938, 41. doi:10.3847/1538-4357/ac8b77, arXiv:2208.10958.

Dainotti, M.G., De Simone, B., Schiavone, T., Montani, G., Rinaldi, E., Lambiase, G., Bogdan, M., Ugale, S., 2022c. On the evolution of the hubble constant with the sne ia pantheon sample and baryon acoustic oscillations: a feasibility study for grb-cosmology in 2030. *Galaxies* 10, 24.

Dainotti, M.G., Del Vecchio, R., Shigehiro, N., Capozziello, S., 2015. Selection Effects in Gamma-Ray Burst Correlations: Consequences on the Ratio between Gamma-Ray Burst and Star Formation Rates. *The Astrophysical Journal* 800, 31. doi:10.1088/0004-637X/800/1/31, arXiv:1412.3969.

Dainotti, M.G., Fabrizio Cardone, V., Capozziello, S., Ostrowski, M., Willingale, R., 2011. Study of Possible Systematics in the  $L^*_{\chi-T^*_a}$  Correlation of Gamma-ray Bursts. *The Astrophysical Journal* 730, 135. doi:10.1088/0004-637X/730/2/135, arXiv:1101.1676.

Dainotti, M.G., Lenart, A., Sarracino, G., Nagataki, S., Capozziello, S., Fraija, N., 2020b. The x-ray fundamental plane of the platinum sample, the kilonovae, and the sne ib/c associated with grbs. *The Astrophysical Journal* 904, 97.

Dainotti, M.G., Lenart, A.Ł., Fraija, N., Nagataki, S., Warren, D.C., De Simone, B., Srinivasaragavan, G., Mata, A., 2021. Closure relations during the plateau emission of swift grbs and the fundamental plane. *Publications of the Astronomical Society of Japan* 73, 970–1000.

Dainotti, M.G., Lenart, A.Ł., Sarracino, G., Nagataki, S., Capozziello, S., Fraija, N., 2020a. The X-Ray Fundamental Plane of the Platinum Sample, the Kilonovae, and the SNe Ib/c Associated with GRBs. *The Astrophysical Journal* 904, 97. doi:10.3847/1538-4357/abbe8a, arXiv:2010.02092.

Dainotti, M.G., Livermore, S., Kann, D.A., Li, L., Oates, S., Yi, S., Zhang, B., Gendre, B., Cenko, B., Fraija, N., 2020b. The Optical Luminosity-Time Correlation for More than 100 Gamma-Ray Burst Afterglows. *The As-*

- rophysical Journal Letters 905, L26. doi:10.3847/2041-8213/abcda9, arXiv:2011.14493.
- Dainotti, M.G., Nagataki, S., Maeda, K., Postnikov, S., Pian, E., 2017. A study of gamma ray bursts with afterglow plateau phases associated with supernovae. *Astronomy and Astrophysics* 600, A98. doi:10.1051/0004-6361/201628384, arXiv:1612.02917.
- Dainotti, M.G., Nielson, V., Sarracino, G., Rinaldi, E., Nagataki, S., Capozziello, S., Gnedin, O.Y., Bargiacchi, G., 2022g. Optical and X-ray GRB Fundamental Planes as cosmological distance indicators. *Monthly Notices of the Royal Astronomical Society* 514, 1828–1856. doi:10.1093/mnras/stac1141, arXiv:2203.15538.
- Dainotti, M.G., Petrosian, V., Singal, J., Ostrowski, M., 2013. Determination of the Intrinsic Luminosity Time Correlation in the X-Ray Afterglows of Gamma-Ray Bursts. *The Astrophysical Journal* 774, 157. doi:10.1088/0004-637X/774/2/157, arXiv:1307.7297.
- Dainotti, M.G., Postnikov, S., Hernandez, X., Ostrowski, M., 2016. A Fundamental Plane for Long Gamma-Ray Bursts with X-Ray Plateaus. *The Astrophysical Journal Letters* 825, L20. doi:10.3847/2041-8205/825/2/L20, arXiv:1604.06840.
- Dainotti, M.G., Sarracino, G., Capozziello, S., 2022b. Gamma-ray bursts, supernovae ia, and baryon acoustic oscillations: A binned cosmological analysis. *Publications of the Astronomical Society of Japan* 74, 1095–1113.
- Dainotti, M.G., Sharma, R., Narendra, A., Levine, D., Rinaldi, E., Pollo, A., Bhatta, G., 2023b. A stochastic approach to reconstruct gamma-ray-burst light curves. *The Astrophysical Journal Supplement Series* 267, 42.
- Dainotti, M.G., Singal, J., Ostrowski, M., et al., 2013. Determination of the intrinsic luminosity time correlation in the x-ray afterglows of gamma-ray bursts. *The Astrophysical Journal* 774, 157.
- Dainotti, M.G., Willingale, R., Capozziello, S., Fabrizio Cardone, V., Ostrowski, M., 2010. Discovery of a Tight Correlation for Gamma-ray Burst Afterglows with “Canonical” Light Curves. *The Astrophysical Journal Letters* 722, L215–L219. doi:10.1088/2041-8205/722/2/L215, arXiv:1009.1663.
- Dainotti, M.G., Young, S., Li, L., Levine, D., Kalinowski, K.K., Kann, D.A., Tran, B., Zambrano-Tapia, L., Zambrano-Tapia, A., Cenko, S.B., Fuentes, M., Sánchez-Vázquez, E.G., Oates, S.R., Fraija, N., Becerra, R.L., Watson, A.M., Butler, N.R., González, J.J., Kutuyev, A.S., Lee, W.H., Prochaska, J.X., Ramirez-Ruiz, E., Richer, M.G., Zola, S., 2022b. The Optical Two- and Three-dimensional Fundamental Plane Correlations for Nearly 180 Gamma-Ray Burst Afterglows with Swift/UVOT, RATIR, and the Subaru Telescope. *The Astrophysical Journal Supplement Series* 261, 25. doi:10.3847/1538-4365/ac7c64, arXiv:2203.12908.
- Demianenko, M., Malanchev, K., Samorodova, E., Sysak, M., Shiriaev, A., Derkach, D., Hushchyn, M., 2023. Understanding of the properties of neural network approaches for transient light curve approximations. *Astronomy & Astrophysics* 677, A16.
- Duncan, R.C., Thompson, C., 1992. Formation of Very Strongly Magnetized Neutron Stars: Implications for Gamma-Ray Bursts. *The Astrophysical Journal Letters* 392, L9. doi:10.1086/186413.
- Evans, P., Beardmore, A., Page, K., Osborne, J., O’Brien, P., Willingale, R., Starling, R., Burrows, D.N., Godet, O., Vetere, L., et al., 2009. Methods and results of an automatic analysis of a complete sample of swift-xrt observations of grbs. *Monthly Notices of the Royal Astronomical Society* 397, 1177–1201.
- Evans, P.A., Beardmore, A.P., Page, K.L., Osborne, J.P., O’Brien, P.T., Willingale, R., Starling, R.L.C., Burrows, D.N., Godet, O., Vetere, L., Racusin, J., Goad, M.R., Wiersema, K., Angelini, L., Capalbi, M., Chincarini, G., Gehrels, N., Kennea, J.A., Margutti, R., Morris, D.C., Mountford, C.J., Paganini, C., Perri, M., Romano, P., Tanvir, N., 2009. Methods and results of an automatic analysis of a complete sample of Swift-XRT observations of GRBs. *Monthly Notices of the Royal Astronomical Society* 397, 1177–1201. doi:10.1111/j.1365-2966.2009.14913.x, arXiv:0812.3662.
- Evans, P.A., Beardmore, A.P., Page, K.L., Tyler, L.G., Osborne, J.P., Goad, M.R., O’Brien, P.T., Vetere, L., Racusin, J., Morris, D., Burrows, D.N., Capalbi, M., Perri, M., Gehrels, N., Romano, P., 2007. An online repository of Swift/XRT light curves of  $\gamma$ -ray bursts. *Astronomy & Astrophysics* 469, 379–385. doi:10.1051/0004-6361:20077530, arXiv:0704.0128.
- Gehrels, N., Chincarini, G., Giommi, P., Mason, K.O., Nousek, J.A., Wells, A.A., White, N.E., Barthelmy, S.D., Burrows, D.N., Cominsky, L.R., Hurley, K.C., Marshall, F.E., Mészáros, P., Roming, P.W.A., Angelini, L., Barbier, L.M., Belloni, T., Campana, S., Caraveo, P.A., Chester, M.M., Citterio, O., Cline, T.L., Cropper, M.S., Cummings, J.R., Dean, A.J., Feigelson, E.D., Fenimore, E.E., Frail, D.A., Fruchter, A.S., Garmire, G.P., Gendreau, K., Ghisellini, G., Greiner, J., Hill, J.E., Hunsberger, S.D., Krimm, H.A., Kulkarni, S.R., Kumar, P., Lebrun, F., Lloyd-Ronning, N.M., Markwardt, C.B., Mattson, B.J., Mushotzky, R.F., Norris, J.P., Osborne, J., Paczynski, B., Palmer, D.M., Park, H.S., Parsons, A.M., Paul, J., Rees, M.J., Reynolds, C.S., Rhoads, J.E., Sasseen, T.P., Schaefer, B.E., Short, A.T., Smale, A.P., Smith, I.A., Stella, L., Tagliaferri, G., Takahashi, T., Tashiro, M., Townsley, L.K., Tueller, J., Turner, M.J.L., Vietri, M., Voges, W., Ward, M.J., Willingale, R., Zerbi, F.M., Zhang, W.W., 2004. The Swift Gamma-Ray Burst Mission. *The Astrophysical Journal* 611, 1005–1020. doi:10.1086/422091, arXiv:astro-ph/0405233.
- Gehrels, N., Ramirez-Ruiz, E., Fox, D.B., 2009. Gamma-Ray Bursts in the Swift Era. *Annual Review of Astronomy and Astrophysics* 47, 567–617. doi:10.1146/annurev.astro.46.060407.145147, arXiv:0909.1531.
- Gorbovskey, E.S., Lipunova, G.V., Lipunov, V.M., Kornilov, V.G., Belinski, A.A., Shatskiy, N.I., Tyurina, N.V., Kuvshinov, D.A., Balanutsa, P.V., Chazov, V.V., Kuznetsov, A., Zimmukhov, D.S., Kornilov, M.V., Sankovich, A.V., Krylov, A., Ivanov, K.I., Chvalaev, O., Poleschuk, V.A., Konstantinov, E.N., Gress, O.A., Yazev, S.A., Budnev, N.M., Krushinski, V.V., Zolozhnik, I.S., Popov, A.A., Tlatov, A.G., Parhomenko, A.V., Dromidontov, D.V., Senik, V., Yurkov, V.V., Sergienko, Y.P., Varda, D., Kudelina, I.P., Castro-Tirado, A.J., Gorosabel, J., Sánchez-Ramírez, R., Jelinek, M., Tello, J.C., 2012. Prompt, early and afterglow optical observations of five  $\gamma$ -ray bursts: GRB 100901A, GRB 100902A, GRB 100905A, GRB 100906A and GRB 101020A. *Monthly Notices of the Royal Astronomical Society* 421, 1874–1890. doi:10.1111/j.1365-2966.2012.20195.x, arXiv:1111.3625.
- Graves, A., Fernández, S., Schmidhuber, J., 2005. Bidirectional lstm networks for improved phoneme classification and recognition, in: *International conference on artificial neural networks*, Springer. pp. 799–804.
- Hjorth, J., Bloom, J.S., 2012. The Gamma-Ray Burst - Supernova Connection, in: *Chapter 9 in “Gamma-Ray Bursts*, pp. 169–190.
- Hjorth, J., Sollerman, J., Møller, P., Fynbo, J.P.U., Woosley, S.E., Kouveliotou, C., Tanvir, N.R., Greiner, J., Andersen, M.I., Castro-Tirado, A.J., Castro Cerón, J.M., Fruchter, A.S., Gorosabel, J., Jakobsson, P., Kaper, L., Klose, S., Masetti, N., Pedersen, H., Pedersen, K., Pian, E., Palazzi, E., Rhoads, J.E., Rol, E., van den Heuvel, E.P.J., Vreeswijk, P.M., Watson, D., Wijers, R.A.M.J., 2003. A very energetic supernova associated with the  $\gamma$ -ray burst of 29 March 2003. *Nature* 423, 847–850. doi:10.1038/nature01750, arXiv:astro-ph/0306347.
- Hochreiter, S., Schmidhuber, J., 1997. Long short-term memory. *Neural computation* 9, 1735–80. doi:10.1162/neco.1997.9.8.1735.
- Huber, S., Suyu, S., 2024. Holismokes–xii. time-delay measurements of strongly lensed type ia supernovae using a long short-term memory network. arXiv preprint arXiv:2403.08029.
- Kann, D.A., Klose, S., Zeh, A., 2006. Signatures of Extragalactic Dust in Pre-Swift GRB Afterglows. *The Astrophysical Journal* 641, 993–1009. doi:10.1086/500652, arXiv:astro-ph/0512575.
- Kann, D.A., Klose, S., Zhang, B., Covino, S., Butler, N.R., Malesani, D., Nakar, E., Wilson, A.C., Antonelli, L.A., Chincarini, G., Cobb, B.E., D’Avanzo, P., D’Elia, V., Della Valle, M., Ferrero, P., Fugazza, D., Gorosabel, J., Israel, G.L., Mannucci, F., Piranomonte, S., Schulze, S., Stella, L., Tagliaferri, G., Wiersema, K., 2011. The Afterglows of Swift-era Gamma-Ray Bursts. II. Type I GRB versus Type II GRB Optical Afterglows. *The Astrophysical Journal* 734, 96. doi:10.1088/0004-637X/734/2/96, arXiv:0804.1959.
- Kann, D.A., Klose, S., Zhang, B., Malesani, D., Nakar, E., Pozanenko, A., Wilson, A.C., Butler, N.R., Jakobsson, P., Schulze, S., Andreev, M., Antonelli, L.A., Bikmaev, I.F., Biryukov, V., Böttcher, M., Burenin, R.A., Castro Cerón, J.M., Castro-Tirado, A.J., Chincarini, G., Cobb, B.E., Covino, S., D’Avanzo, P., D’Elia, V., Della Valle, M., de Ugarte Postigo, A., Efimov, Y., Ferrero, P., Fugazza, D., Fynbo, J.P.U., Gäfalk, M., Grundahl, F., Gorosabel, J., Gupta, S., Guziy, S., Hafizov, B., Hjorth, J., Holmjem, K., Ibrahimov, M., Im, M., Israel, G.L., Jelinek, M., Jensen, B.L., Karimov, R., Khamitov, I.M., Kiziloğlu, Ü., Klunko, E., Kubánek, P., Kutuyev, A.S., Laursen, P., Levan, A.J., Mannucci, F., Martin, C.M., Mescheryakov, A., Mirabal, N., Norris, J.P., Ovaldsen, J.E., Paraficz, D., Pavlenko, E., Piranomonte, S., Rossi, A., Rummyantsev, V., Salinas, R., Sergeev, A., Sharapov, D., Sollerman, J., Stecklum, B., Stella, L., Tagliaferri, G., Tanvir, N.R., Telt-



- ing, J., Testa, V., Updike, A.C., Volnova, A., Watson, D., Wiersema, K., Xu, D., 2010. The Afterglows of Swift-era Gamma-ray Bursts. I. Comparing pre-Swift and Swift-era Long/Soft (Type II) GRB Optical Afterglows. *The Astrophysical Journal* 720, 1513–1558. doi:10.1088/0004-637X/720/2/1513, arXiv:0712.2186.
- Kingma, D.P., Ba, J., 2014. Adam: A method for stochastic optimization. arXiv:1412.6980.
- Kouveliotou, C., Meegan, C.A., Fishman, G.J., Bhat, N.P., Briggs, M.S., Koshut, T.M., Paciesas, W.S., Pendleton, G.N., 1993. Identification of Two Classes of Gamma-Ray Bursts. *The Astrophysical Journal Letters* 413, L101. doi:10.1086/186969.
- Kumar, P., Duran, R.B., 2010. External forward shock origin of high-energy emission for three gamma-ray bursts detected by fermi. *Monthly Notices of the Royal Astronomical Society* 409, 226–236.
- Kumar, P., Narayan, R., Johnson, J.L., 2008. Properties of Gamma-Ray Burst Progenitor Stars. *Science* 321, 376. doi:10.1126/science.1159003, arXiv:0807.0445.
- Kumar, P., Zhang, B., 2015. The physics of gamma-ray bursts & relativistic jets. *Physics Reports* 561, 1–109. doi:10.1016/j.physrep.2014.09.008, arXiv:1410.0679.
- Levan, A.J., Tanvir, N.R., Jakobsson, P., Chapman, R., Hjorth, J., Priddey, R.S., Fynbo, J.P.U., Hurley, K., Jensen, B.L., Johnson, R., Gorosabel, J., Castro-Tirado, A.J., Jarvis, M., Watson, D., Wiersema, K., 2008. On the nature of the short-duration GRB 050906. *Monthly Notices of the Royal Astronomical Society* 384, 541–547. doi:10.1111/j.1365-2966.2007.11953.x, arXiv:0705.1705.
- Li, L., Liang, E.W., Tang, Q.W., Chen, J.M., Xi, S.Q., Lü, H.J., Gao, H., Zhang, B., Zhang, J., Yi, S.X., Lu, R.J., Lü, L.Z., Wei, J.Y., 2012. A Comprehensive Study of Gamma-Ray Burst Optical Emission. I. Flares and Early Shallow-decay Component. *The Astrophysical Journal* 758, 27. doi:10.1088/0004-637X/758/1/27, arXiv:1203.2332.
- Li, L., Wang, Y., Shao, L., Wu, X.F., Huang, Y.F., Zhang, B., Ryde, F., Yu, H.F., 2018a. A Large Catalog of Multiwavelength GRB Afterglows. I. Color Evolution and Its Physical Implication. *The Astrophysical Journal Supplement* 234, 26. doi:10.3847/1538-4365/aaa02a, arXiv:1712.03704.
- Li, L., Wu, X.F., Huang, Y.F., Wang, X.G., Tang, Q.W., Liang, Y.F., Zhang, B.B., Wang, Y., Geng, J.J., Liang, E.W., Wei, J.Y., Zhang, B., Ryde, F., 2015. A Correlated Study of Optical and X-Ray Afterglows of GRBs. *The Astrophysical Journal* 805, 13. doi:10.1088/0004-637X/805/1/13, arXiv:1503.00976.
- Li, L., Wu, X.F., Lei, W.H., Dai, Z.G., Liang, E.W., Ryde, F., 2018b. Constraining the Type of Central Engine of GRBs with Swift Data. *The Astrophysical Journal Supplement* 236, 26. doi:10.3847/1538-4365/aabaf3, arXiv:1712.09390.
- Liang, E.W., Zhang, B.B., Zhang, B., 2007. A Comprehensive Analysis of Swift XRT Data. II. Diverse Physical Origins of the Shallow Decay Segment. *The Astrophysical Journal* 670, 565–583. doi:10.1086/521870, arXiv:0705.1373.
- Liu, H., Liu, C., Wang, J.T., Wang, H., 2019. Predicting solar flares using a long short-term memory network. *The Astrophysical Journal* 877, 121.
- Lyman, J.D., Levan, A.J., Tanvir, N.R., Fynbo, J.P.U., McGuire, J.T.W., Perley, D.A., Angus, C.R., Bloom, J.S., Conselice, C.J., Fruchter, A.S., Hjorth, J., Jakobsson, P., Starling, R.L.C., 2017. The host galaxies and explosion sites of long-duration gamma ray bursts: Hubble Space Telescope near-infrared imaging. *Monthly Notices of the Royal Astronomical Society* 467, 1795–1817. doi:10.1093/mnras/stx220, arXiv:1701.05925.
- MacFadyen, A.I., Woosley, S.E., 1999. Collapsars: Gamma-Ray Bursts and Explosions in “Failed Supernovae”. *The Astrophysical Journal* 524, 262–289. doi:10.1086/307790, arXiv:astro-ph/9810274.
- Margutti, R., Zaninoni, E., Bernardini, M.G., Chincarini, G., Pasotti, F., Guidorzi, C., Angelini, L., Burrows, D.N., Capalbi, M., Evans, P.A., Gehrels, N., Kennea, J., Mangano, V., Moretti, A., Nousek, J., Osborne, J.P., Page, K.L., Perri, M., Racusin, J., Romano, P., Sbarufatti, B., Stafford, S., Stamatikos, M., 2013. The prompt-afterglow connection in gamma-ray bursts: a comprehensive statistical analysis of Swift X-ray light curves. *Monthly Notices of the Royal Astronomical Society* 428, 729–742. doi:10.1093/mnras/sts066, arXiv:1203.1059.
- Mazets, E., Golenetskii, S., Il’Inskii, V., Panov, V., Aptekar, R., Gur’yan, Y.A., Proskura, M., Sokolov, I., Sokolova, Z.Y., Kharitonova, T., et al., 1981. Catalog of cosmic gamma-ray bursts from the konus experiment data. *Astrophysics and Space Science* 80, 3–83.
- Melandri, A., Covino, S., Rogantini, D., Salvaterra, R., Sbarufatti, B., Bernardini, M.G., Campana, S., D’Avanzo, P., D’Elia, V., Fugazza, D., Ghirlanda, G., Ghisellini, G., Nava, L., Vergani, S.D., Tagliaferri, G., 2014. Optical and X-ray rest-frame light curves of the BAT6 sample. *Astronomy & Astrophysics* 565, A72. doi:10.1051/0004-6361/201323361, arXiv:1403.3245.
- Metzger, B.D., Giannios, D., Thompson, T.A., Bucciantini, N., Quataert, E., 2011. The protomagnetar model for gamma-ray bursts. *Monthly Notices of the Royal Astronomical Society* 413, 2031–2056. doi:10.1111/j.1365-2966.2011.18280.x, arXiv:1012.0001.
- Mirza, M., Osindero, S., 2014. Conditional generative adversarial nets. URL: <https://arxiv.org/abs/1411.1784>, arXiv:1411.1784.
- Narayan, R., Paczynski, B., Piran, T., 1992. Gamma-Ray Bursts as the Death Throes of Massive Binary Stars. *The Astrophysical Journal Letters* 395, L83. doi:10.1086/186493, arXiv:astro-ph/9204001.
- Narendra, A., Dainotti, M., Sarkar, M., Lenart, A., Bogdan, M., Pollo, A., Zhang, B., Rabeda, A., Petrosian, V., Kazunari, I., 2024. Grb redshift estimation using machine learning and the associated web-app. arXiv preprint arXiv:2410.13985.
- Nousek, J.A., Kouveliotou, C., Grupe, D., Page, K.L., Granot, J., Ramirez-Ruiz, E., Patel, S.K., Burrows, D.N., Mangano, V., Barthelmy, S., Beardmore, A.P., Campana, S., Capalbi, M., Chincarini, G., Cusumano, G., Falcone, A.D., Gehrels, N., Giommi, P., Goad, M.R., Godet, O., Hurkett, C.P., Kennea, J.A., Moretti, A., O’Brien, P.T., Osborne, J.P., Romano, P., Tagliaferri, G., Wells, A.A., 2006. Evidence for a Canonical Gamma-Ray Burst Afterglow Light Curve in the Swift XRT Data. *The Astrophysical Journal* 642, 389–400. doi:10.1086/500724, arXiv:astro-ph/0508332.
- Oates, S.R., Page, M.J., De Pasquale, M., Schady, P., Breeveld, A.A., Holland, S.T., Kuin, N.P.M., Marshall, F.E., 2012. A correlation between the intrinsic brightness and average decay rate of Swift/UVOT gamma-ray burst optical/ultraviolet light curves. *Monthly Notices of the Royal Astronomical Society* 426, L86–L90. doi:10.1111/j.1745-3933.2012.01331.x, arXiv:1208.1856.
- O’Brien, P.T., Willingale, R., Osborne, J., Goad, M.R., Page, K.L., Vaughan, S., Rol, E., Beardmore, A., Godet, O., Hurkett, C.P., Wells, A., Zhang, B., Kobayashi, S., Burrows, D.N., Nousek, J.A., Kennea, J.A., Falcone, A., Grupe, D., Gehrels, N., Barthelmy, S., Cannizzo, J., Cummings, J., Hill, J.E., Krimm, H., Chincarini, G., Tagliaferri, G., Campana, S., Moretti, A., Giommi, P., Perri, M., Mangano, V., LaParola, V., 2006. The Early X-Ray Emission from GRBs. *The Astrophysical Journal* 647, 1213–1237. doi:10.1086/505457, arXiv:astro-ph/0601125.
- Paczynski, B., 1998. Are Gamma-Ray Bursts in Star-Forming Regions? *The Astrophysical Journal Letters* 494, L45–L48. doi:10.1086/311148, arXiv:astro-ph/9710086.
- Panaitescu, A., Kumar, P., 2000. Analytic light curves of gamma-ray burst afterglows: homogeneous versus wind external media. *The Astrophysical Journal* 543, 66.
- Panaitescu, A., Vestrand, W.T., 2008. Taxonomy of gamma-ray burst optical light curves: identification of a salient class of early afterglows. *Monthly Notices of the Royal Astronomical Society* 387, 497–504. doi:10.1111/j.1365-2966.2008.13231.x, arXiv:0803.1872.
- Panaitescu, A., Vestrand, W.T., 2011. Optical afterglows of gamma-ray bursts: peaks, plateaus and possibilities. *Monthly Notices of the Royal Astronomical Society* 414, 3537–3546. doi:10.1111/j.1365-2966.2011.18653.x, arXiv:1009.3947.
- Perna, R., Lazzati, D., Cantiello, M., 2018. Ultra-long Gamma-Ray Bursts from the Collapse of Blue Supergiant Stars: An End-to-end Simulation. *The Astrophysical Journal* 859, 48. doi:10.3847/1538-4357/aabcc1, arXiv:1803.04983.
- Perna, R., Lazzati, D., Giacomazzo, B., 2016. Short Gamma-Ray Bursts from the Merger of Two Black Holes. *The Astrophysical Journal Letters* 821, L18. doi:10.3847/2041-8205/821/1/L18, arXiv:1602.05140.
- Piran, T., 1999. Gamma-ray bursts and the fireball model. *Physics Reports* 314, 575–667.
- Piro, L., Amati, L., Antonelli, L.A., Butler, R.C., Costa, E., Cusumano, G., Feroci, M., Frontera, F., Heise, J., in ’t Zand, J.J.M., Molendi, S., Muller, J., Nicastro, L., Orlandini, M., Owens, A., Parmar, A.N., Soffitta, P., Tavani, M., 1998. Evidence for a late-time outburst of the X-ray afterglow of GB970508 from BeppoSAX. *Astronomy and Astrophysics* 331, L41–L44. arXiv:astro-ph/9710355.
- Postnikov, S., Dainotti, M.G., Hernandez, X., Capozziello, S., 2014. Non-

- parametric study of the evolution of the cosmological equation of state with sneia, bao, and high-redshift grbs. *The Astrophysical Journal* 783, 126.
- Racusin, J., Liang, E., Burrows, D.N., Falcone, A., Sakamoto, T., Zhang, B., Zhang, B., Evans, P., Osborne, J., 2009. Jet breaks and energetics of swift gamma-ray burst x-ray afterglows. *The Astrophysical Journal* 698, 43.
- Racusin, J.L., Liang, E.W., Burrows, D.N., Falcone, A., Sakamoto, T., Zhang, B.B., Zhang, B., Evans, P., Osborne, J., 2009. Jet Breaks and Energetics of Swift Gamma-Ray Burst X-Ray Afterglows. *The Astrophysical Journal* 698, 43–74. doi:10.1088/0004-637X/698/1/43, arXiv:0812.4780.
- Roming, P.W.A., Kennedy, T.E., Mason, K.O., Nousek, J.A., Ahr, L., Bingham, R.E., Broos, P.S., Carter, M.J., Hancock, B.K., Huckle, H.E., Hunsberger, S.D., Kawakami, H., Killough, R., Koch, T.S., McLelland, M.K., Smith, K., Smith, P.J., Soto, J.C., Boyd, P.T., Breeveld, A.A., Holland, S.T., Ivanushkina, M., Pryzby, M.S., Still, M.D., Stock, J., 2005. The Swift Ultra-Violet/Optical Telescope. *Space Science Review* 120, 95–142. doi:10.1007/s11214-005-5095-4, arXiv:astro-ph/0507413.
- Rowlinson, A., Gompertz, B.P., Dainotti, M., O'Brien, P.T., Wijers, R.A.M.J., van der Horst, A.J., 2014. Constraining properties of GRB magnetar central engines using the observed plateau luminosity and duration correlation. *Monthly Notices of the Royal Astronomical Society* 443, 1779–1787. doi:10.1093/mnras/stu1277, arXiv:1407.1053.
- Ryan, G., Van Eerten, H., Piro, L., Troja, E., 2020. Gamma-ray burst afterglows in the multimessenger era: numerical models and closure relations. *The Astrophysical Journal* 896, 166.
- Sakamoto, T., Barthelmy, S.D., Barbier, L., Cummings, J.R., Fenimore, E.E., Gehrels, N., Hullinger, D., Krimm, H.A., Markwardt, C.B., Palmer, D.M., Parsons, A.M., Sato, G., Stamatikos, M., Tueller, J., Ukwatta, T.N., Zhang, B., 2008. The First Swift BAT Gamma-Ray Burst Catalog. *The Astrophysical Journal Supplement Series* 175, 179–190. doi:10.1086/523646, arXiv:0707.4626.
- Sakamoto, T., Hill, J.E., Yamazaki, R., Angelini, L., Krimm, H.A., Sato, G., Swindell, S., Takami, K., Osborne, J.P., 2007. Evidence of Exponential Decay Emission in the Swift Gamma-Ray Bursts. *The Astrophysical Journal* 669, 1115–1129. doi:10.1086/521640, arXiv:0707.2170.
- Si, S.K., Qi, Y.Q., Xue, F.X., Liu, Y.J., Wu, X., Yi, S.X., Tang, Q.W., Zou, Y.C., Wang, F.F., Wang, X.G., 2018. The Three-parameter Correlations About the Optical Plateaus of Gamma-Ray Bursts. *The Astrophysical Journal* 863, 50. doi:10.3847/1538-4357/aad08a, arXiv:1807.00241.
- Sourav, S., Shukla, A., Dwivedi, R., Singh, K., 2023. Predicting missing light curves of gamma-ray bursts with bidirectional-1stm: An approach for enhanced analysis. arXiv preprint arXiv:2310.02602.
- Srinivasaragavan, G.P., Dainotti, M.G., Fraija, N., Hernandez, X., Nagataki, S., Lenart, A., Bowden, L., Wagner, R., 2020. On the investigation of the closure relations for gamma-ray bursts observed by swift in the post-plateau phase and the grb fundamental plane. *The Astrophysical Journal* 903, 18.
- Srinivasaragavan, G.P., Dainotti, M.G., Fraija, N., Hernandez, X., Nagataki, S., Lenart, A., Bowden, L., Wagner, R., 2020. On the Investigation of the Closure Relations for Gamma-Ray Bursts Observed by Swift in the Post-plateau Phase and the GRB Fundamental Plane. *The Astrophysical Journal* 903, 18. doi:10.3847/1538-4357/abb702, arXiv:2009.06740.
- Tagliaferri, G., Goad, M., Chincarini, G., Moretti, A., Campana, S., Burrows, D.N., Perri, M., Barthelmy, S.D., Gehrels, N., Krimm, H., Sakamoto, T., Kumar, P., Mészáros, P.I., Kobayashi, S., Zhang, B., Angelini, L., Banat, P., Beardmore, A.P., Capalbi, M., Covino, S., Cusumano, G., Giommi, P., Godet, O., Hill, J.E., Kennea, J.A., Mangano, V., Morris, D.C., Nousek, J.A., O'Brien, P.T., Osborne, J.P., Paganì, C., Page, K.L., Romano, P., Stella, L., Wells, A., 2005. An unexpectedly rapid decline in the X-ray afterglow emission of long  $\gamma$ -ray bursts. *Nature* 436, 985–988. doi:10.1038/nature03934, arXiv:astro-ph/0506355.
- Tak, D., Omodei, N., Uhm, Z.L., Racusin, J., Asano, K., McEnery, J., 2019. Closure relations of gamma-ray bursts in high energy emission. *The Astrophysical Journal* 883, 134.
- Tang, C.H., Huang, Y.F., Geng, J.J., Zhang, Z.B., 2019. Statistical Study of Gamma-Ray Bursts with a Plateau Phase in the X-Ray Afterglow. *The Astrophysical Journal Supplement Series* 245, 1. doi:10.3847/1538-4365/ab4711, arXiv:1905.07929.
- Thompson, C., 1994. A Model of Gamma-Ray Bursts. *Monthly Notices of the Royal Astronomical Society* 270, 480. doi:10.1093/mnras/270.3.480.
- Torkzadehmahani, R., Kairouz, P., Paten, B., 2019. Dp-cgan: Differentially private synthetic data and label generation, in: *Proceedings of the IEEE/CVF Conference on Computer Vision and Pattern Recognition Workshops*, pp. 0–0.
- Troja, E., Cusumano, G., O'Brien, P.T., Zhang, B., Sbarufatti, B., Mangano, V., Willingale, R., Chincarini, G., Osborne, J.P., Marshall, F.E., Burrows, D.N., Campana, S., Gehrels, N., Guidorzi, C., Krimm, H.A., La Parola, V., Liang, E.W., Mineo, T., Moretti, A., Page, K.L., Romano, P., Tagliaferri, G., Zhang, B.B., Page, M.J., Schady, P., 2007. Swift Observations of GRB 070110: An Extraordinary X-Ray Afterglow Powered by the Central Engine. *The Astrophysical Journal* 665, 599–607. doi:10.1086/519450, arXiv:astro-ph/0702220.
- Usov, V.V., 1992. Millisecond pulsars with extremely strong magnetic fields as a cosmological source of gamma-ray bursts. *Nature* 357, 472–474. doi:10.1038/357472a0.
- van Paradijs, J., Groot, P.J., Galama, T., Kouveliotou, C., Strom, R.G., Telling, J., Rutten, R.G.M., Fishman, G.J., Meegan, C.A., Pettini, M., Tanvir, N., Bloom, J., Pedersen, H., Nørdgaard-Nielsen, H.U., Linden-Vørnle, M., Melnick, J., Van der Steene, G., Bremer, M., Naber, R., Heise, J., in't Zand, J., Costa, E., Feroci, M., Piro, L., Frontera, F., Zavattini, G., Nicastro, L., Palazzi, E., Bennett, K., Hanlon, L., Parmar, A., 1997. Transient optical emission from the error box of the  $\gamma$ -ray burst of 28 February 1997. *Nature* 386, 686–689. doi:10.1038/386686a0.
- Vestrand, W.T., Woźniak, P.R., Wren, J.A., Fenimore, E.E., Sakamoto, T., White, R.T., Casperson, D., Davis, H., Evans, S., Galassi, M., McGowan, K.E., Schier, J.A., Asa, J.W., Barthelmy, S.D., Cummings, J.R., Gehrels, N., Hullinger, D., Krimm, H.A., Markwardt, C.B., McLean, K., Palmer, D., Parsons, A., Tueller, J., 2005. A link between prompt optical and prompt  $\gamma$ -ray emission in  $\gamma$ -ray bursts. *Nature* 435, 178–180. doi:10.1038/nature03515, arXiv:astro-ph/0503521.
- Vestrand, W.T., Wren, J.A., Panaitescu, A., Woźniak, P.R., Davis, H., Palmer, D.M., Vianello, G., Omodei, N., Xiong, S., Briggs, M.S., Elphick, M., Paciasas, W., Rosing, W., 2014. The Bright Optical Flash and Afterglow from the Gamma-Ray Burst GRB 130427A. *Science* 343, 38–41. doi:10.1126/science.1242316, arXiv:1311.5489.
- Wang, F.Y., Hu, J.P., Zhang, G.Q., Dai, Z.G., 2022. Standardized Long Gamma-Ray Bursts as a Cosmic Distance Indicator. *Astrophys. J.* 924, 97. doi:10.3847/1538-4357/ac3755, arXiv:2106.14155.
- Willingale, R., O'Brien, P., Osborne, J., Godet, O., Page, K., Goad, M., Burrows, D.N., Zhang, B., Rol, E., Gehrels, N., et al., 2007. Testing the standard fireball model of gamma-ray bursts using late x-ray afterglows measured by swift. *The Astrophysical Journal* 662, 1093.
- Woosley, S.E., 1993. Gamma-Ray Bursts from Stellar Mass Accretion Disks around Black Holes. *The Astrophysical Journal* 405, 273. doi:10.1086/172359.
- Woosley, S.E., Bloom, J.S., 2006. The Supernova Gamma-Ray Burst Connection. *Annual Review of Astronomy and Astrophysics* 44, 507–556. doi:10.1146/annurev.astro.43.072103.150558, arXiv:astro-ph/0609142.
- Woosley, S.E., Heger, A., 2006. The Progenitor Stars of Gamma-Ray Bursts. *The Astrophysical Journal* 637, 914–921. doi:10.1086/498500, arXiv:astro-ph/0508175.
- Xu, B., Wang, N., Chen, T., Li, M., 2015. Empirical evaluation of rectified activations in convolutional network. URL: <https://arxiv.org/abs/1505.00853>, arXiv:1505.00853.
- Yonetoku, D., Doi, A., Mihara, T., Matsuhara, H., Sakamoto, T., Tsumura, K., Ioka, K., Arimoto, M., Enoto, T., Fujimoto, K., et al., 2024. High-z gamma-ray bursts unraveling the dark ages and extreme space-time mission-hiz-gundam, in: *Space Telescopes and Instrumentation 2024: Ultraviolet to Gamma Ray*, SPIE. pp. 618–626.
- Yuan, W., Zhang, C., Chen, Y., Ling, Z., 2022. The einstein probe mission, in: *Handbook of X-ray and Gamma-ray Astrophysics*. Springer, pp. 1–30.
- Zaninoni, E., Bernardini, M.G., Margutti, R., Oates, S., Chincarini, G., 2013. Gamma-ray burst optical light-curve zoo: comparison with X-ray observations. *Astronomy and Astrophysics* 557, A12. doi:10.1051/0004-6361/201321221, arXiv:1303.6924.
- Zeh, A., Klose, S., Kann, D.A., 2006. Gamma-Ray Burst Afterglow Light Curves in the Pre-Swift Era: A Statistical Study. *The Astrophysical Journal* 637, 889–900. doi:10.1086/498442, arXiv:astro-ph/0509299.
- Zhang, B., Fan, Y.Z., Dyks, J., Kobayashi, S., Mészáros, P., Burrows, D.N., Nousek, J.A., Gehrels, N., 2006. Physical Processes Shaping Gamma-Ray Burst X-Ray Afterglow Light Curves: Theoretical Implications from the Swift X-Ray Telescope Observations. *The Astrophysical Journal* 642, 354–370. doi:10.1086/500723, arXiv:astro-ph/0508321.

Zhang, B., Mészáros, P., 2001. Gamma-Ray Burst Afterglow with Continuous Energy Injection: Signature of a Highly Magnetized Millisecond Pulsar. *The Astrophysical Journal Letters* 552, L35–L38. doi:10.1086/320255, arXiv:astro-ph/0011133.

Zhang, B., Mészáros, P., 2004. Gamma-Ray Bursts: progress, problems & prospects. *Int J Mod Phys A* 19, 2385–2472. doi:10.1142/S0217751X0401746X, arXiv:astro-ph/0311321.

Zhang, B., Zhang, B.B., Liang, E.W., Gehrels, N., Burrows, D.N., Mészáros, P., 2007. Making a Short Gamma-Ray Burst from a Long One: Implications for the Nature of GRB 060614. *The Astrophysical Journal Letters* 655, L25–L28. doi:10.1086/511781, arXiv:astro-ph/0612238.

Zhao, L., Zhang, B., Gao, H., Lan, L., Lü, H., Zhang, B., 2019. The Shallow Decay Segment of GRB X-Ray Afterglow Revisited. *The Astrophysical Journal* 883, 97. doi:10.3847/1538-4357/ab38c4, arXiv:1908.01561.